

1 **Classifying marine faults for hazard assessment offshore**  
2 **Israel: A new approach based on fault size and vertical**  
3 **displacement**

4 May Laor<sup>1,2\*</sup>, Zohar Gvirtzman<sup>1,2</sup>

5 <sup>1</sup> Geological Survey of Israel, Yesha'yahu Leibowitz 32, Jerusalem, Israel

6 <sup>2</sup> Institute of Earth Sciences, The Hebrew University of Jerusalem, Israel

7 \* Correspondence to: May Laor (may.laor@mail.huji.ac.il)

## 8 **Abstract**

9 For many countries, the methodology for offshore geohazard mitigation lags far behind  
10 the well-established onshore methodology. Particularly complicated is the assessment  
11 of fault hazard in the marine environment. The determination of whether a fault is  
12 “active” or not requires ultra-high-resolution seismic surveys and multiple coring and  
13 unfortunately, frequently ends with uncertain results. Moreover, if a pipeline must cross  
14 a fault, it is not enough to determine whether the fault is active; slip rates are needed  
15 for resistant planning.

16 Here we suggest a new approach for fault hazard assessment for the master planning of  
17 infrastructure. We provide planners a way to choose a route that will cross the least  
18 hazardous faults; these faults will then be investigated in site-specific surveys for slip  
19 rates that will allow seismic design. Instead of following the onshore practice that is  
20 hard to implement in the marine environment, we suggest taking advantage of the  
21 marine environment where seismic data is commonly better in quantity and quality.  
22 Based on existing industrial 3D seismic surveys, we measure for each fault in the study  
23 area the amount of its recent (in our specific case, 350 ka) vertical displacement and the  
24 size of its plane. According to these two independently measured quantities, we classify  
25 the faults into three hazard levels. This allows planners to choose infrastructure routes  
26 that cross the least hazardous faults at an early stage of planning and direct them to sites  
27 that need further investigation.

28 Our case study is the Israeli continental slope, where numerous salt-related, thin-  
29 skinned, normal faults dissect the seabed, forming tens of meters high scarps. A  
30 particular hazardous zone is the upper slope south of the Dor disturbance, where a series  
31 of big listric faults rupture the seabed in an area where the sedimentation rate is four

32 times faster than the displacement rate. We suggest that this indicates exceptionally fast  
33 creep, seismic rupture, or rapid tremor and slip episodes.

34

## 35 **1. Introduction**

36 The need for geohazard assessment in the marine environment is increasing globally  
37 due to the growing number of infrastructures laid on the seafloor. To mitigate marine  
38 geohazards, numerous studies have been conducted in many world basins (Georgia  
39 Basin (Barrie et al., 2005); Sea of Marmara (Armijo et al., 2005); Gulf of Mexico (Prior  
40 and Hooper, 1999); offshore California (Clark et al., 1985, and the ref in); Norwegian  
41 Sea (Shmatkova et al., 2015); Italian continental margins (Chiocci and Ridente, 2011),  
42 and more). Some of these studies focus on submarine landslides, and when faults are  
43 considered, they are sometimes treated as static seabed obstacles. Note, however, that  
44 even extremely accurate mapping of the seafloor does not provide the information  
45 needed to determine whether the fault is active or not.

46 Onshore, the criteria for fault activity is well established – “active faults” are defined  
47 as faults that have moved one or more times in the last 11,000 years (Bryant and Hart,  
48 2007). To determine if a specific fault is active, the continuation or displacement of  
49 Holocene markers is examined in outcrops or trenches.

50 In the marine environment, such an approach is much more complicated and requires  
51 high-resolution seismic surveys and core analyses (Posamentier, 2000; Kvalstad, 2007;  
52 Hough et al., 2011). Commonly a site-specific survey includes four steps (Prior and  
53 Hooper, 1999; Angell et al., 2003): (a) Mapping the seafloor, (b) establishing a chrono-  
54 stratigraphic scheme by tying high-resolution seismic data to dated horizons in  
55 boreholes, (c) structural mapping of the fault and displacement measurements, (d)  
56 geological interpretation and quantification. This commonly used approach is  
57 problematic because each survey requires months of work and frequently yields  
58 uncertain results.

59 One practical option is to define all faults rupturing the seabed as active faults in the  
60 absence of age information (On, 2016). This approach is based on the rationale that  
61 faults are likely active if they are identified at the seabed despite sedimentation. Note,  
62 however, that fault scarps can remain hundreds of thousands of years on the seabed  
63 without any additional jump if the sedimentation rate is lower than the displacement  
64 rate.

65 Another approach is to apply a Probabilistic Fault Displacement Hazard Assessment  
66 (PFDHA, Wong and Stepp, 1998; Youngs et al., 2003; Angell et al., 2003), analogs to  
67 the practice developed for earthquake ground motion prediction (PSHA, Cornell, 1968,  
68 1971). Such analysis provides a graph showing the annual frequency calculated for  
69 various displacement values. This probabilistic approach requires assumptions  
70 regarding (1) creep versus seismic slip and (2) the number of seismic events that had  
71 produced an observed displacement. In the case studied here (offshore Israel), we do  
72 not know if the studied faults produce earthquakes at all (maybe they only creep).  
73 Furthermore, if they produce earthquakes, we do not have any information about the  
74 magnitudes-frequency relationships. Thus, it seems that this approach will not yield  
75 robust results in our case.

76 The goal of this study is to provide a practical and relatively fast solution for early-stage  
77 planning of marine infrastructure that must cross a faulted zone. For instance, there is  
78 no choice in the case studied here, and planning requires a route that will cross the least  
79 hazardous faults. For this, we need criteria to determine the relative fault hazard level.  
80 We base this determination on the amount of recent displacement and the size of the  
81 fault plane. We assume that bigger faults with larger past displacements have a greater  
82 potential for larger future ruptures.

83 Our analysis takes advantage of the wealth of high-resolution seismic data frequently  
84 available offshore. Instead of investing in multiple coring to find out whether or not  
85 each specific fault in the study area displaces Holocene (~11 ka) horizons (a practice  
86 that frequently fails to provide an answer), we measure the displacement of a 350 ka  
87 horizon, and the area of the fault plane. These two parameters are tough to measure in  
88 seismic data usually available on land and are easily measured in high-resolution  
89 surveys frequently available offshore.

## 90 **2. Scientific background**

### 91 *2.1. Geological history of the Levant Basin*

92 The Levant Basin was formed in the late Paleozoic and early Mesozoic, alongside the  
93 opening of the Tethys Ocean that had separated Africa from Eurasia (Garfunkel and  
94 Almagor, 1984; Garfunkel, 1988,1998; Robertson, 1998). At that time, several rifting  
95 phases created a system of horsts and grabens spreading from the northern Negev  
96 northwestwards into the Levant basin (Bein and Gvirtzman, 1977; Garfunkel and  
97 Almagor, 1984; Garfunkel, 1988,1998; Robertson, 1998). After the rifting stage,  
98 approximately at the end of the Early Jurassic (~180 Ma), the Levant continental  
99 margins turned passive and continued to accumulate sediments for more than 100  
100 million years (Gvirtzman and Garfunkel, 1997, 1998; Steinberg et al., 2008; Bar et al.,  
101 2013).

102 At the end of the Turonian and the beginning of the Santonian (~84 Ma), a change in  
103 the relative movement between Africa and Eurasia led to a change in the stress regime  
104 and folding along the "Syrian arc" began (Krenkel, 1924; Henson, 1951; De-Sitter,  
105 1962; Freund, 1975; Reches and Hoexter, 1981; Eyal and Reches, 1983; Sagy et al.,  
106 2018).

107 About 35 million years ago, a large area, including east Africa and northern Arabia,  
108 started rising above sea level. This process provided large amounts of clastic sediments  
109 to the Levant Basin, where the sedimentation rate increased significantly (Gvirtzman et  
110 al., 2008; Steinberg et al., 2011; Avni et al., 2012; Bar et al., 2016, 2013). These clastic  
111 sediments compose the Saqiye Group, which thickens from tens of hundreds of meters  
112 in the Israeli coasts to 1.5 km in the continental shelf area (Gvirtzman and Buchbinder,  
113 1978), and 6 km in the deep Levant Basin (Steinberg et al., 2011).

114 About 6 million years ago, the connection between the Mediterranean Sea and the  
115 Atlantic Ocean was restricted during a short event termed the Messinian Salinity Crisis  
116 (MSC). During the crisis, the sea level dropped, and a few km thick evaporite sequence  
117 accumulated in the entire Mediterranean Sea (e.g., Ryan and Hsü, 1973; Hsü et al.,  
118 1973). The salt sequence offshore Israel is nearly 2-km-thick in the deepest portion of  
119 the basin, thinning landwards and nearly pinching out to zero beneath the continental  
120 slope (Ryan and Cita, 1978; Mart and Gai, 1982; Gradmann et al., 2005; Bertoni and  
121 Cartwright, 2006; Netzeband et al., 2006; Gvirtzman et al., 2013, 2017).

122 In the Pliocene, the Nile, one of the largest rivers in the world, supplied a huge amount  
123 of sediments to the eastern Mediterranean that buried the Messinian salt and produced  
124 a giant delta with a well-developed deep-sea fan (Masclé et al., 2001). Alongshore  
125 currents transporting sediments from the Nile Delta through the Sinai coast to the Israeli  
126 coast gradually formed the continental shelf offshore Israel (Gvirtzman and  
127 Buchbinder, 1978; Goldsmith and Golik, 1980; Carmel et al., 1985; Stanley, 1989;  
128 Tibor et al., 1992; Buchbinder et al., 1993; Golik, 1993, 2002; Buchbinder and  
129 Zilberman, 1997; Perlin and Kit, 1999; Ben-Gai et al., 2005; Zviely et al., 2006, 2007;  
130 Klein et al., 2007; Schattner et al., 2015; Schattner and Lazar, 2016; Zucker et al.,

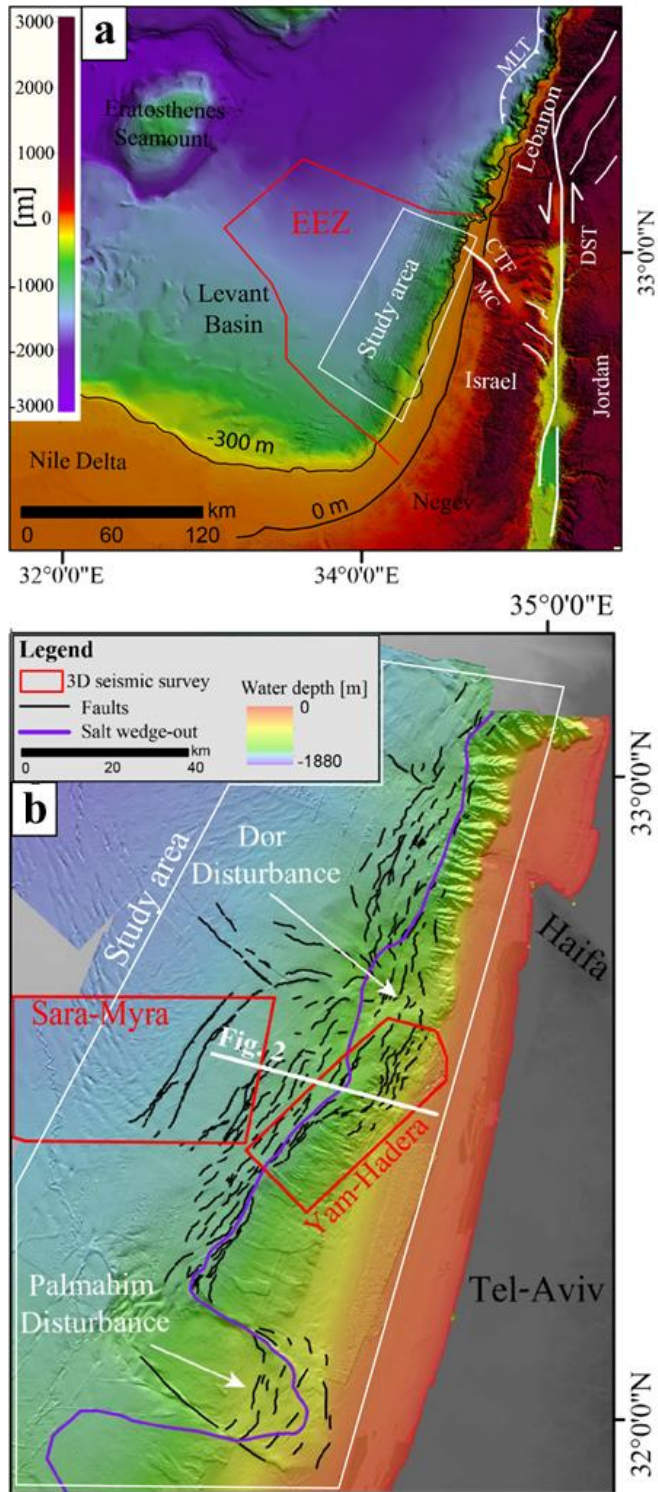
131 2021). The slope of this continental shelf is currently faulted by faults, which are the  
132 target of this study.

## 133 2.2. *Regional tectonic activity*

134 It is generally agreed that the Levant continental margin is passive since the Mid-  
135 Jurassic (Garfunkel, 1988; Gvirtzman et al., 2008) with no deep-seated active faults  
136 south of Mount Carmel (Fig. 1a). Neev et al. (1973), and Neev, (1975) debated this  
137 consensus suggesting that an active fault, which they named the Pelusium Line, runs  
138 all along the Israeli continental margin. On the other side, Garfunkel and Derin, (1984)  
139 and Garfunkel, (1988), argued that all faults crossing the Plio-Quaternary section  
140 offshore Israel are thin-skinned and salt-related. Nearly 30 years later, based on better  
141 seismic data, Gvirtzman et al. (2008) and Gvirtzman and Steinberg, (2012) showed that  
142 a continental margin fault zone (CMFZ) does exist approximately at the same location  
143 marked by Neev et al. (1973), but this line stopped operating in the Miocene. The deep-  
144 seated faults along the CMFZ (~Pelusium Line) are sealed with Miocene strata and do  
145 not reach the surface.

146 Moving northwards to offshore northern Israel and Lebanon, the current tectonic  
147 activity is different. The Carmel-Tirza Fault (CTF, Fig. 1a), a branch of the Dead Sea  
148 Transform (DST), disrupts the continental margin off the Galilee (Kafri and Folkman,  
149 1981; Garfunkel and Almagor, 1984; Ginzburg and Ben-Avraham, 1987; Schattner et  
150 al., 2006; Sharon et al., 2020). In addition, the Mount Lebanon Thrust (Fig. 1a) disrupts  
151 the continental margin offshore Lebanon and produces earthquakes, such as the 551  
152 A.D. M=7.5 Beirut-Tripoli earthquake (Elias et al., 2007).





153

154 *Figure 1: Location maps. (a) Regional setting - bathymetry and topography from Hall (1994).*  
 155 *Abbreviations: EEZ - Israel's Exclusive Economic Zone. CTZ - Carmel-Tirza Fault, DST - Dead*  
 156 *Sea Transform. MLT - Mount Lebanon Thrust Fault. (b) The studied area with thin-skinned*  
 157 *faults in black after Gvirtzman et al. (2015). Red polygons are borders of seismic surveys*  
 158 *mentioned in the text.*

159

160           2.3. *Thin-skinned, salt-related normal faulting along the Israeli*  
161                                   *continental slope*

162 Unlike the deep-seated faults that stopped operating in the Miocene and do not reach  
163 the seabed, numerous thin-skinned normal faults rupture the seafloor all along the  
164 Israeli continental slope (Fig. 1b), creating steep steps that are tens of meters high  
165 (Almagor and Garfunkel, 1979; Garfunkel et al., 1979; Mart and Gai, 1982; Almagor,  
166 1984; Garfunkel, 1984; Garfunkel and Almagor, 1984; Tibor et al., 1992; Gradmann et  
167 al., 2005; Martinez et al., 2005; Bertoni and Cartwright, 2005, 2006; Netzeband et al.,  
168 2006; Mart and Ryan, 2007; Cartwright and Jackson, 2008; Cartwright et al., 2012;  
169 Gvirtzman et al., 2013, 2015; Katz et al., 2015; Safadi et al., 2017; Gadol et al., 2019).

170 Recently, based on improved bathymetry data, the seabed traced of these faults were  
171 mapped in detail (Gvirtzman et al., 2015; Katz et al., 2015; Kanari et al., 2020), showing  
172 that their scarps are not buried by sediments. This apparently indicates that  
173 displacement rates are higher than burial rates. However, averaged over hundreds of  
174 thousands of years, displacement rates are roughly similar to sedimentation rates  
175 (Elfassi et al., 2019). This indicates that the fault scarps observed on the present seafloor  
176 may have formed by recent instantaneous seismic ruptures (Elfassi et al., 2019) or rapid  
177 episodic motions. In any case, these relatively shallow thin-skinned faults are incapable  
178 of producing large earthquakes (discussed below) because their fault planes are  
179 relatively small compared to crustal faults. The major hazard they pose is surface  
180 rupture, which may as well trigger slumps (Katz et al., 2015).

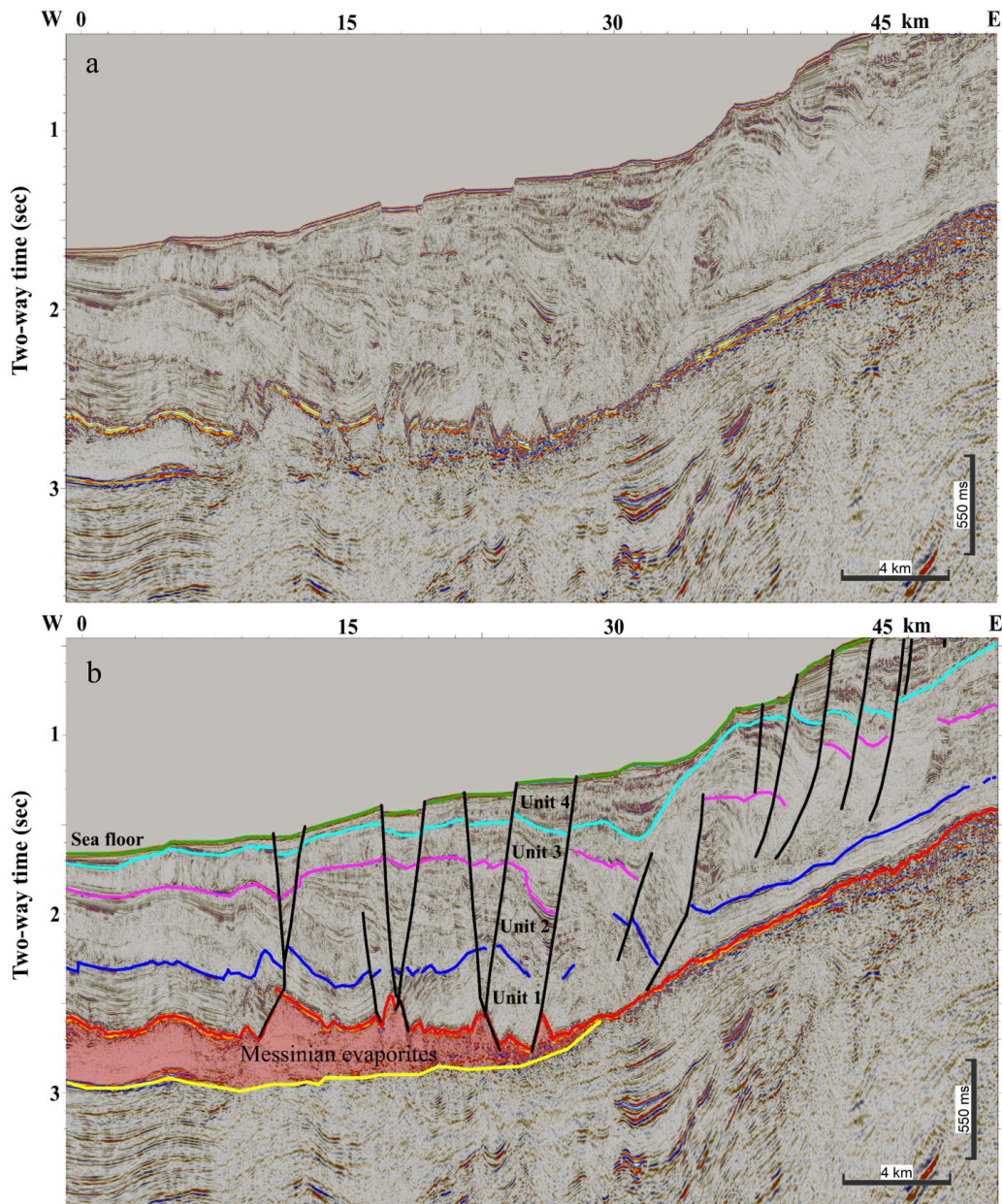
181 The recognition that the thin-skinned faults along the Levant continental margin are  
182 related to salt tectonics has been stated in many studies (Neev et al., 1976; Ben-  
183 Avraham, 1978; Almagor and Hall, 1979; Garfunkel et al., 1979; Mart and Gai, 1982;  
184 Garfunkel, 1984; Garfunkel and Almagor, 1984; Tibor et al., 1992; Gradmann et al.,

185 2005; Martinez et al., 2005; Bertoni and Cartwright, 2006, 2007; Loncke et al., 2006;  
186 Netzeband et al., 2006; Hübscher and Netzeband, 2007; Mart and Ryan, 2007;  
187 Hübscher et al., 2008; Cartwright and Jackson, 2008; Clark and Cartwright, 2009;  
188 Cartwright et al., 2012; Gvirtzman et al., 2013; Gadol et al., 2019; Ben Zeev and  
189 Gvirtzman, 2020; Hamdani et al., 2021). In particular, it has been suggested that  
190 faulting was initiated by basinward salt flow (Gradmann et al., 2005; Bertoni and  
191 Cartwright, 2006, 2015; Allen et al., 2016; Cartwright et al., 2018; Kirkham et al., 2019)  
192 triggered by basinward tilting of the continental margin, as a result of coastal uplift  
193 (Cartwright and Jackson, 2008; Elfassi et al., 2019; Hamdani et al., 2021).

194 The beginning of faulting was initially dated to a relatively broad time interval between  
195 the late Pliocene and the early Pleistocene (e.g., Garfunkel et al., 1979; Almagor, 1984;  
196 Gradmann et al., 2005; Netzeband et al., 2006). Later, based on 3D high-resolution  
197 seismic surveys, Cartwright and Jackson, (2008) showed that offshore central Israel  
198 faulting began in the mid-Pliocene. Then, in the late Pliocene, it spread northward, and  
199 in the early Pleistocene, southward. Elfassi et al. (2019) established a new  
200 chronostratigraphic scheme for the Pliocene-Quaternary section offshore Israel that  
201 allows better fault dating. By combining seismic and bio-stratigraphic data, they  
202 divided the Plio-Quaternary sequence into four units (Fig. 2): Unit 1- Pliocene (5.33-  
203 2.6 Ma); Unit 2- Gelasian (2.6-1.8 Ma); Unit 3- Calabrian-Ionian (1.8-0.35 Ma); and  
204 Unit 4- Ionian-Holocene (<0.35 Ma). Based on the improved Chrono-stratigraphy,  
205 Elfassi et al. (2019) measured displacement rates on several faults offshore central  
206 Israel (in the Sara-Myra survey, Fig. 1b) and concluded that during the Pliocene faulting

207 activity was minor ( $< 4$  m/Ma), then, in the Gelasian, it peaked to rates of  $>100$  m/Ma  
208 (10 cm/ky). Later it decreased to rates of  $\sim 50$  m/My (5 cm/ky).

209 In what follows, we use the chrono-stratigraphy of Elfassi et al. (2019) to map the most  
210 recent horizon (350 ka) in the entire study area (light blue- base Unit 4 in Fig. 2b) and  
211 identify the zones with the most potent recent activity.



212

213 *Figure 2: Uninterpreted (a) and interpreted (b) seismic section across the Levant continental*  
214 *margin offshore Israel (location in Fig. 1b). Chrono- and seismo-stratigraphic of the Pliocene-*  
215 *Quaternary section after Elfassi et al. (2019). Green- Sea floor, Light blue – base Unit 4, purple*  
216 *– base Unit 3, blue – base Unit 2, red – base Unit 1 (and top evaporites), yellow – Base*  
217 *evaporates. Thin-skinned faults in black lines.*

218           2.4.   *The Dor and the Palmahim Disturbances*

219   Two huge (10s of km) thin-skinned, rootless structures were observed in the 1970s  
220   along the Israeli slope – the Palmahim and the Dor Disturbances (Fig. 1b; Garfunkel et  
221   al., 1979; Garfunkel, 1984; Almagor, 1984). Some studies described these disturbances  
222   as deep-seated tectonic structures (e.g., Neev et al., 1976), while others suggested  
223   gravitational instability structures induced by basinward sliding over late Miocene (i.e.,  
224   Messinian evaporites) detachment surface (Garfunkel et al., 1977). According to  
225   Garfunkel, (1984), these disturbances are similar to other gravitationally induced  
226   rootless structures, which are related to the flowage of underlying salt or shale, that are  
227   known in deltas and continental margins in other parts of the world (C. H. Bruce, 1973;  
228   Evamy et al., 1978; Harding and Lowell, 1979; Crans et al., 1980). The Palmahim  
229   structure has been described as a rotational slide, bounded between two translational  
230   faults (Mart et al., 1978; Garfunkel et al., 1979), while the Dor Disturbance seems to be  
231   the focus of a regional deformation zone (Garfunkel, 1984; Gadol et al., 2019).

### 232 **3. Data and Methods**

233 This study aims to map seabed fault scarps and their subsurface continuation.  
234 Accordingly, we start with bathymetry analysis quantifying fault scarps; and then use  
235 seismic data to map faults in the subsurface.

#### 236 *3.1. Bathymetry*

237 The Israel national bathymetry survey provides pixel resolution of 15 m until a water  
238 depth of ~700 m (Sade et al., 2006, 2007) and 50 m between isobaths 700 m and 1700  
239 m (Tibor et al., 2013). In addition, we used bathymetric grids with ~10 m cell size,  
240 derived from four 3D seismic surveys listed in Table 1 (Aviya; Dalit; Yam Hadera; and  
241 Sara-Myra).

242 To quantify the height of fault scarps at the present seafloor, we developed an algorithm  
243 that uses the fault map prepared by Gvirtzman et al. (2015) and automatically calculates  
244 elevation differences from both sides of the fault segment every 50 meters. A fault  
245 segment is a visually mappable lineament in a bathymetric map, regardless of its  
246 connection to other segments in the sub-seabed. The algorithm begins with manually  
247 moving fault segments, marked by Gvirtzman et al. (2015), to their most accurate  
248 location, that is, along the maximal slope of the seabed fault scarp. Then, for each point  
249 along each fault, the algorithm measures the dip angle and the true fault direction (dip  
250 direction), ignoring the possibility that the fault scarp may have changed by erosion  
251 and/or sedimentation. For each point along the faults, the algorithm searches the two  
252 closest points from both sides of the fault according to the true dip direction and the dip  
253 angle. The calculated output includes the three components of the fault movement;  
254 Throw, Heave, and Displacement. This algorithm was applied to all grids described in  
255 Table 1, and the measurements were used for the throw analysis.

256       3.2.   *Seismic reflection data*

257   The seismic data used here include 2D and 3D industrial seismic reflection surveys  
258   processed in the time domain (TWT) and 3D seismic cubes that were pre-stack depth  
259   migrated (Table 1). All surveys were loaded and interpreted using the Kingdom HIS  
260   software. Preliminary mapping of the four seismic units described above was done by  
261   Elfassi et al. (2019). Ben-Zeev and Gvirtzman, (2020) expanded this mapping to cover  
262   Israel's Exclusive Economic Zone (EEZ; Fig. 1a). Here, we recheck and remap these  
263   horizons in detail along the continental slope where faults are common and map these  
264   four units in 3D seismic volumes (Fig. 1b, Table 1).

265           3.2.1.   *Subsurface faults mapping*

266   Each fault with a seabed expression was mapped in the subsurface. When a seismic  
267   volume was available, we mapped the faults in 3D and frequently showed that separate  
268   seabed segments connect in the subsurface. If only the 2D seismic lines were available,  
269   connectivity between segments would sometimes remain uncertain.

270   The subsurface mapping of faults adds several layers of information on top of seabed  
271   mapping: (1) it allows measuring the displacement of dated horizons and thus indicates  
272   the rate of motion; (2) it allows distinguishing between small surface faults that are  
273   minor and small surface faults that connect at the subsurface to large faults; (3) it allows  
274   identifying hidden fault segments, which do not appear on the bathymetry but may  
275   rupture in the future; (4) it provides a 3D view of the fault plane which is essential  
276   for structural analysis (and estimation of potential earthquake magnitudes, if these  
277   faults rupture seismically, see discussion).

278

#	Survey name	Survey type and units	Source	Survey's technical details	Grid cell size	Data available for this study
1	Aviya	Seismic reflection: Depth m	Delek Ltd.	Line spacing: 25 m x 12.5 m Sample interval: 4 ms	10 m	Bathymetry
2	Dalit	Seismic reflection: Depth m	Delek Ltd.	Line spacing: 25 m x 12.5 m Sample interval: 4 ms	10 m	Bathymetry
3	Yam Hadera	Seismic reflection: Depth m	Modiin Energy	Line spacing: 25 m x 12.5 m Sample interval: 5 m	9 m	Seismic (3D), Bathymetry
4	Gabriela	Seismic reflection: Depth m	Modiin Energy	Line spacing: 25 m x 12.5 m Sample interval: 4 m	13 m	Seismic (3D)
5	Sara-Myra	Seismic reflection: Depth m	Modiin Energy + ILDC	Line spacing: 25 m x 12.5 m Sample interval: 3 m	10 m	Seismic (3D), Bathymetry
6	The Israel national bathymetry survey	Multibeam sonar: Depth m	(Sade et al., 2006; Tibor et al., 2013)	15 m x 15 m till water depth of 700 m and 50 m x 50 m till water depth of over 1700 m.	50 m, 15 m	Bathymetry
7	Isramco North Central	Seismic reflection: TWT sec	Isramco	Line spacing: 12.5 m x 12.5 m Sample interval: 4 ms		Seismic (3D)
8	TGS	Seismic reflection: TWT sec	TGS-NOPEC Geophysical Company	Shot interval: 25m Group interval: 12.5 m Sample interval: 2 ms Total line length of ~6000 km.	5-10 km	Seismic (2D)
9	HORIZON	Seismic reflection: TWT sec	Horizon Exploration Limited	Shot interval: 25 m Sample interval: 4 ms		Seismic (2D)
10	SPETRUM	Seismic reflection: TWT sec	Spectrum Energy & info. Tech. Ltd	Shot interval: 50 m Group interval: 12.5 m Sample interval: 4 ms Streamer length: 7200 m		Seismic (2D)

## 280 **4. Results**

### 281 *4.1. Measurements*

#### 282 *4.1.1. Scarp height*

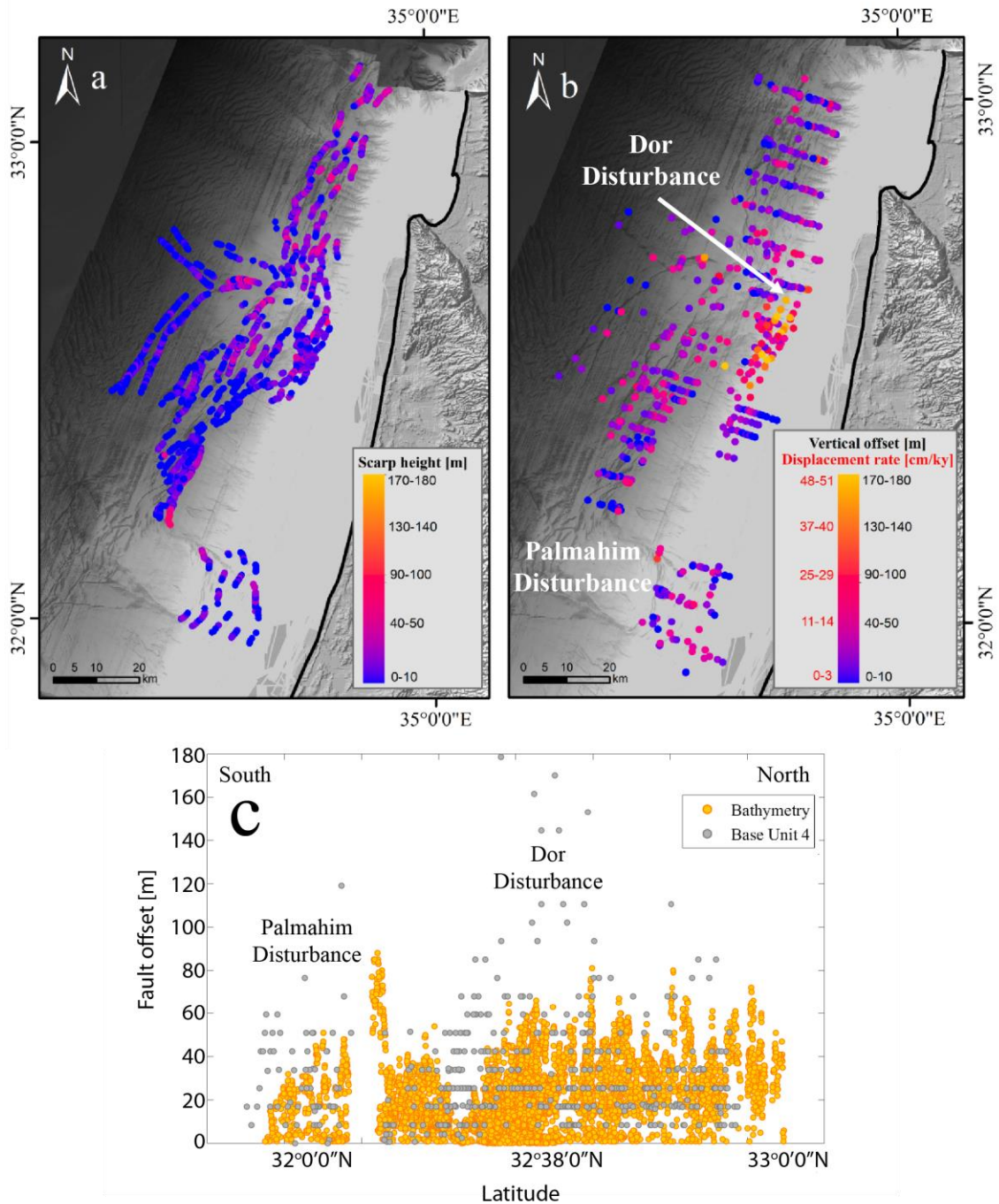
283 Figure 3a shows the heights of seabed scarps measured from both sides of all faults  
 284 every 50 m. The map shows that between the Palmahim and the Dor disturbances, fault  
 285 scarps are relatively low (<20 m), whereas from the Dor disturbance northwards, they



286 are significantly higher (20-90 m). This observation is consistent with extension  
287 measurements that also increases northwards (Cartwright and Jackson, 2008; Ben Zeev  
288 and Gvirtzman, 2020).

#### 289 *4.1.2. Displacement rate*

290 The problem with analyzing bathymetry alone is that faults scarps are reduced by  
291 sedimentation and erosion and do not correctly represent fault displacement. Therefore,  
292 we also measure fault throw along the youngest regionally mappable horizon (base Unit  
293 4, Fig. 3b), which yield displacement rates averaged for the past 350 ky (the best  
294 possible representation of ‘recent’ in the study area). These measurements highlight an  
295 exceptionally active zone in the vicinity of the Dor disturbance with displacement rates  
296 reaching 40-50 cm/ky (Fig. 3b); this anomaly is not detected in the bathymetric analysis  
297 (Fig. 3a), emphasizing the need for subsurface measurements. To further illustrate the  
298 Dor anomaly, Fig. 3c shows a projection of all seabed and subsurface offset  
299 measurements along a south-north section emphasizing peak throws near the Dor  
300 disturbance (@X~32°38'0"N), nearly two times larger than in surrounding areas.



301  
 302 *Figure 3: Vertical offset measurements along faults. (a) Height of seabed scarps derived from*  
 303 *bathymetry analysis. (b) Vertical offsets at the base unit 4 horizon measured from seismic data.*  
 304 *Assigning 350 ka to the base Unit 4 horizon (Elfassi et al., 2019), its vertical offset is*  
 305 *transformed to displacement rate (the left-hand side of the scale bar in b). (c) Vertical offset*  
 306 *measured at the base of unit 4 (gray dots) and scarps height at the seafloor (orange dots). Note*  
 307 *that vertical offsets in bathymetry increase northwards, whereas vertical offsets at the base of*  
 308 *unit 4 increase in the vicinity of the Dor disturbance. Bathymetry from Tibor et al. (2013).*

309

#### 4.1.3. *Sedimentation rate*

310

Considering the 350 ka age of base Unit 4 (Elfassi et al., 2019), recent sedimentation

311

rates (thickness of Unit 4 divided by 350 ky) can be calculated for the entire study area

312

(Fig. 4c). Results indicate relatively low (<60 cm/ky) values in the deep basin,

313

increasing to ~90 cm/ky in the mid-slope and >150 cm/ky along the basinward

314

propagating shelf edge (Ben Zeev and Gvirtzman, 2020). Particularly interesting is the

315

off-shelf area near the Dor disturbance reaching >200 cm/ky (the impact of this

316

observation on fault interpretation is discussed below).

317

In addition to the shelf edge belt, a large thickness of Unit 4 is observed in a deep half-

318

graben separating a prominent dome at the center of the Dor disturbance from the shelf

319

edge (Fig. 4b). The accommodation space created by this half-graben is quickly filled

320

by sediments arriving from the nearby shelf edge. South of the Dor disturbance, the

321

half-graben is separated from the shelf edge (Fig. 5b). North of the disturbance, the two

322

features create a continuous sedimentary package (Fig. 5a). Noteworthy, the listric

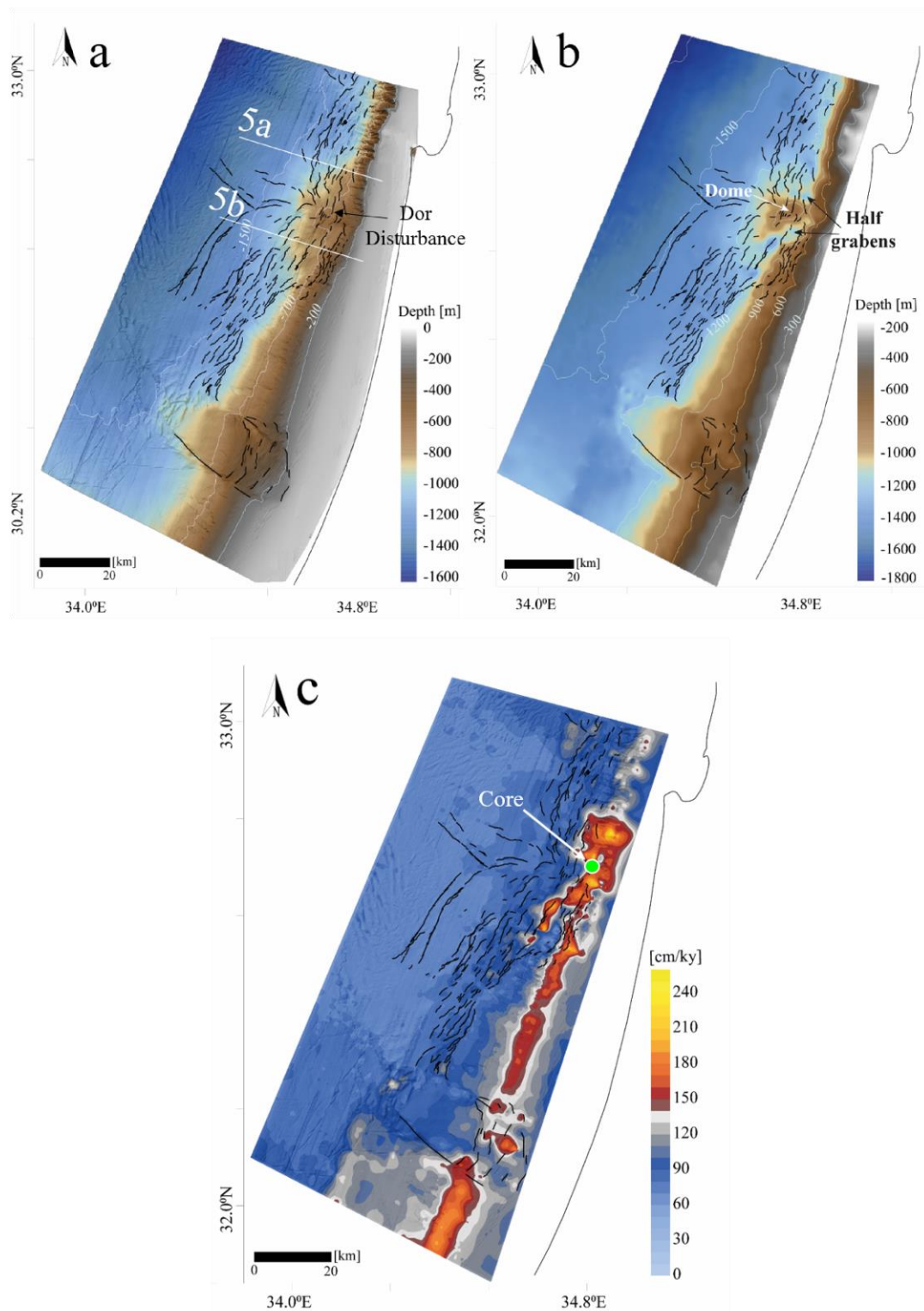
323

faults east of the half-graben are different from all the other faults as will be discussed

324

below.

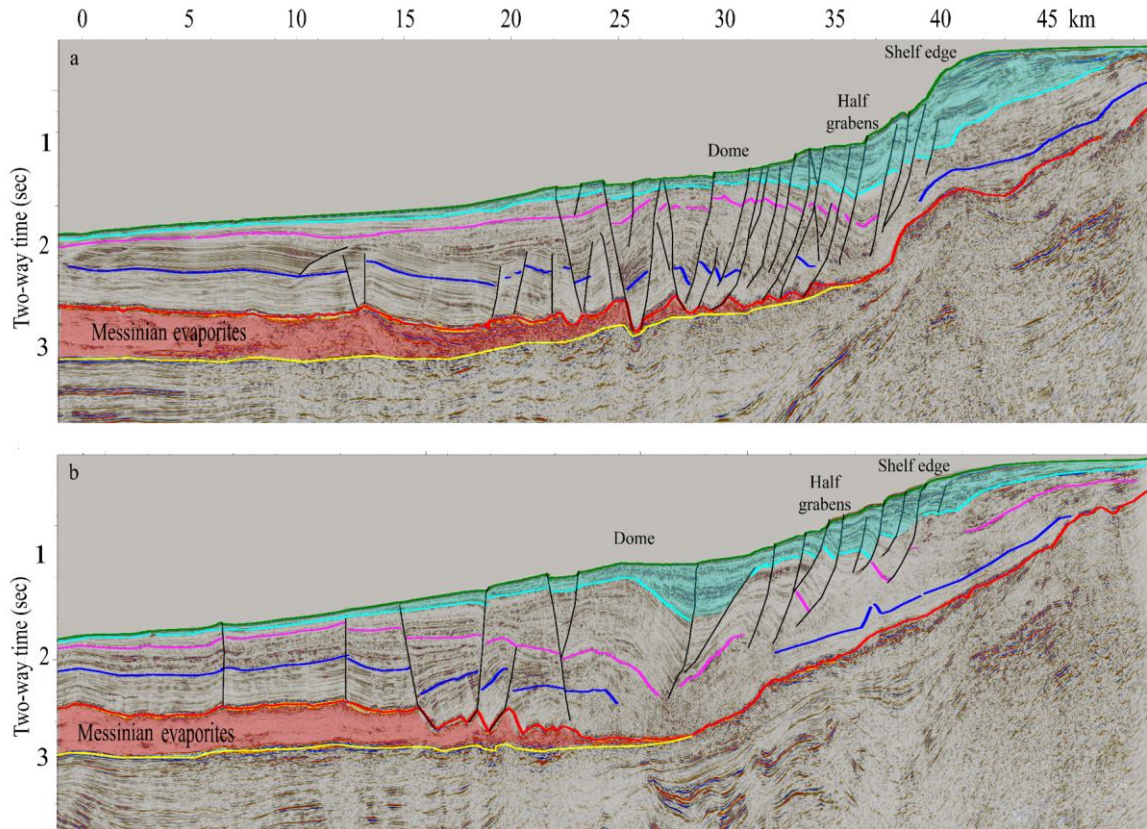
325



326

327 *Figure 4: (a) Faults on bathymetry background (After Tibor et al., 2013). (b) Base unit 4*  
 328 *structure map. (c) Unit 4 sedimentation rate. Half grabens separated the Dor disturbance from*  
 329 *the shelf edge and emphasized its dome shape seen in b. These half grabens are filled with a*  
 330 *thick section of Unit 4 with a sedimentation rate exceeding ~1.8 m/ky (c). A high sedimentation*  
 331 *rate is also observed along the shelf edge, expressing shelf progradation during the past 350*  
 332 *ky.*

333



334

335 *Figure 5: (a) Cross-section north (a) and south (b) of the Dor disturbance (seismic location in*  
 336 *Fig. 4a). Normal faults in black lines. Seismic reflectors as in Fig. 2.*

337

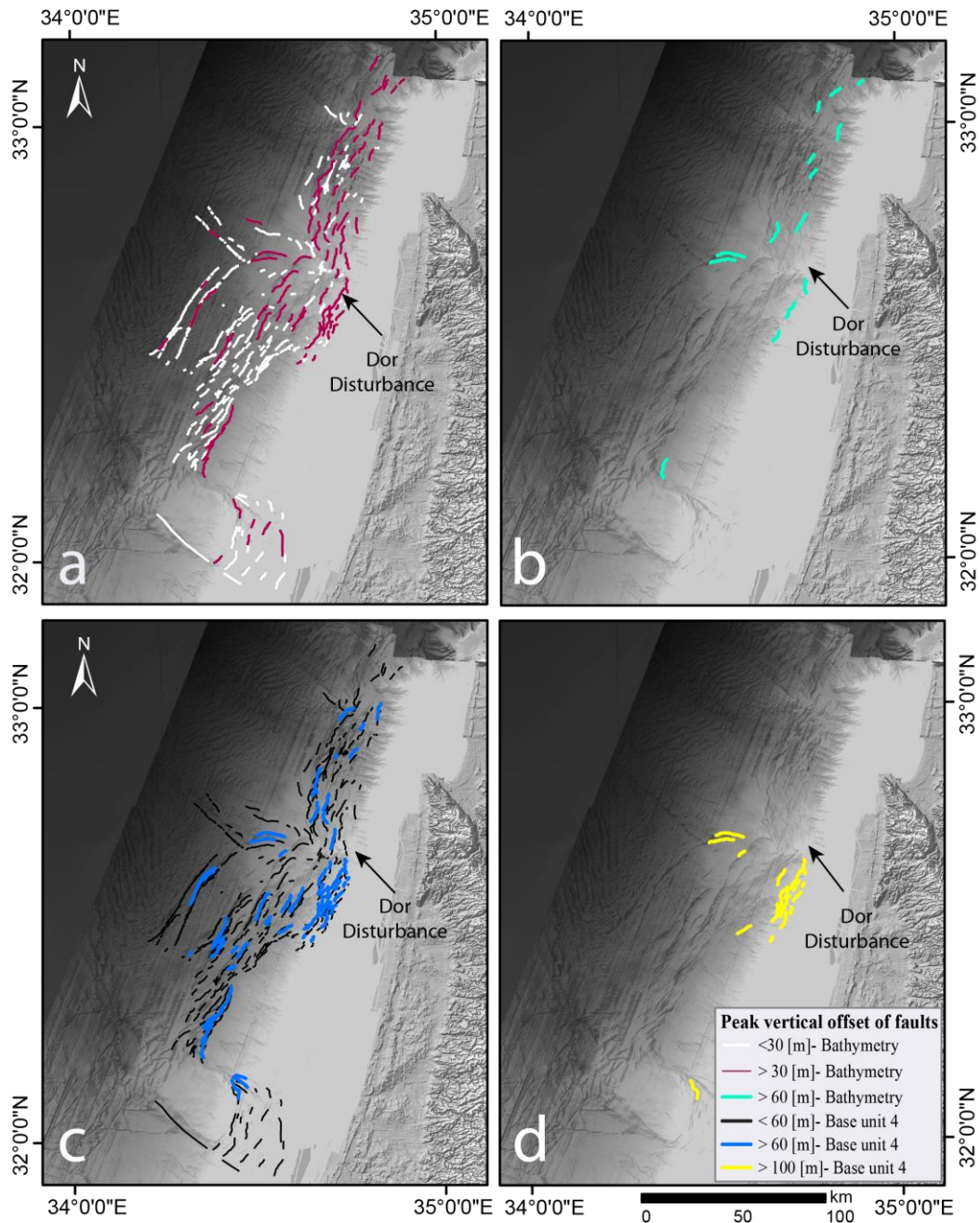
## 338 4.2. Fault classification

### 339 4.2.1. Vertical displacement categories

340 To classify faults according to their vertical displacement, we assign each fault segment  
 341 a single value of maximum throw measured anywhere along it (a) at the seabed (height  
 342 of scarp) and (b) at the base of Unit 4 (vertical offset). Results are presented in Fig. 6  
 343 in three colors – white represents faults producing seabed scarps <30 m; red 30-60 m;  
 344 and turquoise represents faults with seabed scarps >60 m. This illustration is consistent  
 345 with Fig. 3, showing that seabed fault scarps higher than 30 m (red) are more common  
 346 near Dor and northwards (Fig. 6a). In contrast, fault scarps higher than 60 m (turquoise)  
 347 are observed only north of Dor (Fig. 6b) with the exception of one outlier near the  
 348 Palmahim Disturbance. Noteworthy, the threshold values of 30 m and 60 m were  
 349 defined for convenience, such that all three groups will include a reasonable number of

350 faults, and the third group with exceptionally high values will be smaller. If needed,  
351 these threshold values can be changed.

352 Consistent with our hypothesis that fault scarps are decreased by sedimentation and  
353 erosion, classification according to vertical offsets at the base of Unit 4 (Fig. 6c,d)  
354 portrays a different picture with peak vertical displacements in the vicinity of the Dor  
355 disturbance without increasing northward trend (again, one outlier near Palmahim). In  
356 particular, we highlight the faults bounding the Dor disturbance from the east (Fig. 6d),  
357 where large throws ( $>100$  m) at the base of Unit 4 are observed. These faults coincide  
358 with the listric faults mentioned above (Fig. 5b). Uncommonly, these faults form seabed  
359 scarps higher than 60 m (Fig. 6b) despite the exceptionally high sedimentation rate  
360 observed at that location (Fig. 4c).



361

362 *Figure 6: Fault classification by vertical throw after assigning each fault segment a single*  
 363 *value, representing the maximum vertical displacement measured anywhere along it. (a) Faults*  
 364 *forming seabed scarps smaller (white) and higher (red) than 30 meters. (b) Faults forming*  
 365 *seabed scarps larger than 60 meters (turquoise). (c) Faults displacing base Unit 4 by more*  
 366 *than 60 m (blue) and smaller than 60 meters (black). (d) Faults displacing base Unit 4 by more*  
 367 *than 100 m (yellow). Note that faults with the largest vertical throw are concentrated around*  
 368 *the Dor Disturbance. Background in all maps is shaded relief of bathymetry (Tibor et al., 2013).*

369

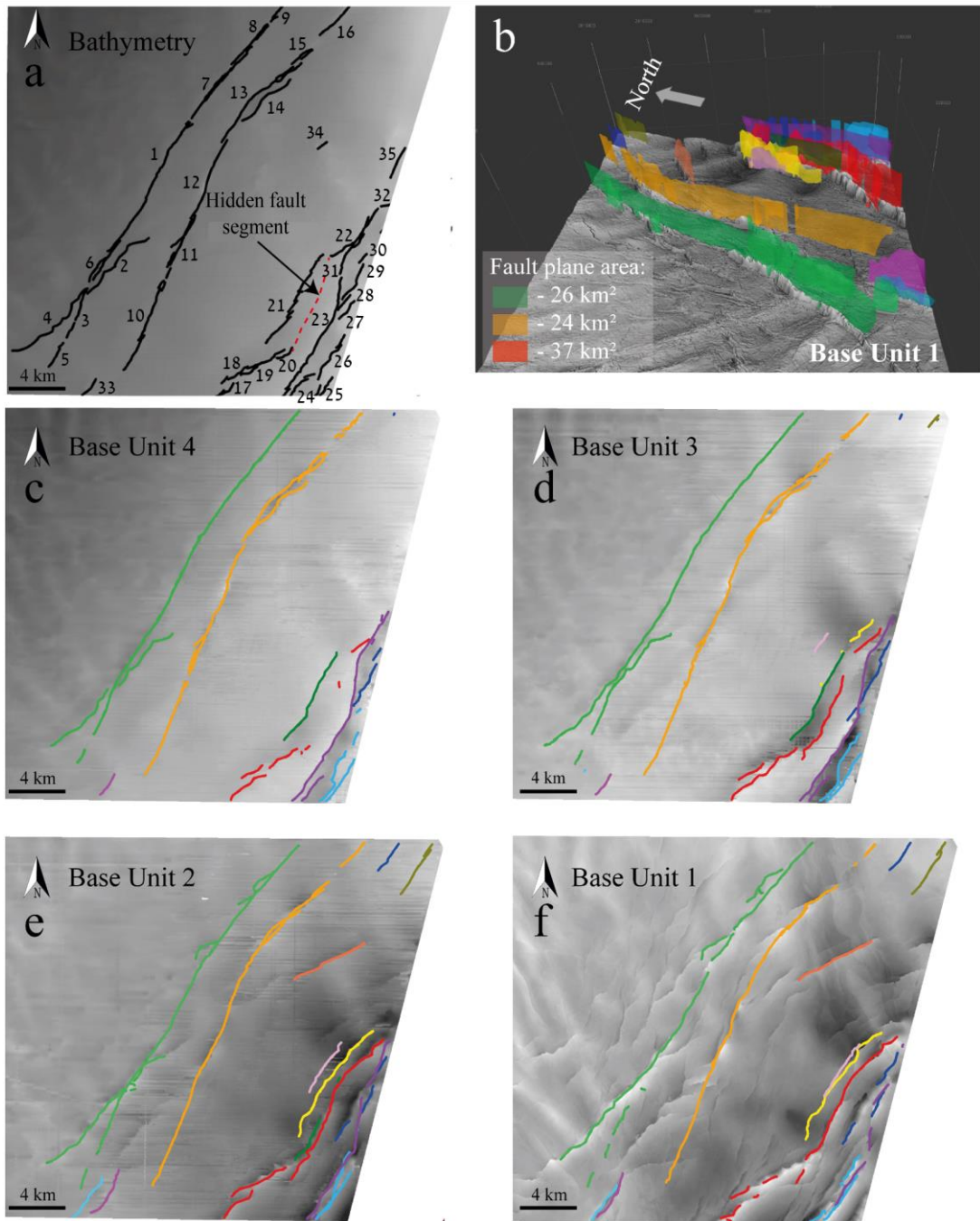
370

#### 371 4.2.2. *Hidden fault segments*

372 To map fault planes in the subsurface and measure their area, we use high-resolution  
373 3D seismic volumes. Figure 7 illustrates that 35 fault segments rupturing the seabed on  
374 the eastern side of the Sara-Myra survey converge at depth to seven major faults.  
375 Noteworthy, a part of the fault marked by red (Fig. 7b) has no surface expression (Fig.  
376 7a). This hidden fault segment ruptures the three lower horizons (Fig. 7d-f), reaching  
377 base Unit 4 in several locations (Fig. 7c) and is unseen at the seabed (Fig. 7a). Namely,  
378 the partial seabed segments do not represent the actual fault size. A similar analysis  
379 conducted for the Yam Hadera seismic survey illustrates that several major fault  
380 segments (marked green, pink, and yellow) are hidden (Fig. 8a,b). The sub-seabed fault  
381 mapping in 3D highlights the segments “missing” in the bathymetry.

382 Figure 8c presents an example of five 3D-mapped faults with their measured plane area.  
383 The red and blue faults are two sides of one graben rooted in the Messinian salt layer  
384 with a relatively minor fault plane area, whereas the pink, yellow and green faults have  
385 a significantly larger fault plane area despite their shallower penetration only to the top  
386 of the Pliocene (base unit 2) horizon (Fig. 8c).



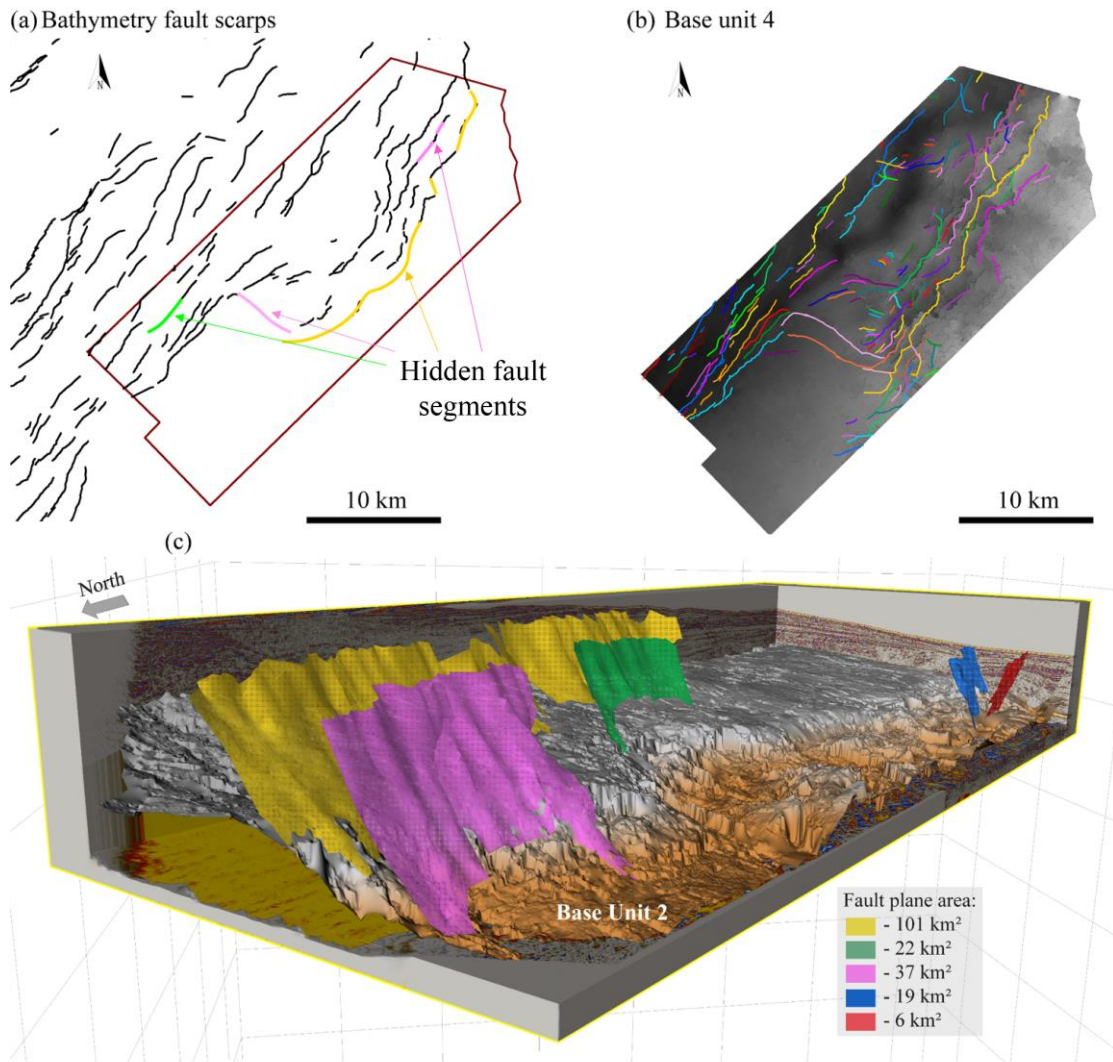


387

388 *Figure 7: Subsurface mapping of fault planes. (a) 35 faults segments rupturing the seabed in*  
 389 *the eastern part of the Sara-Myra survey (location in Fig. 1). (b) A 3D view of fault planes*  
 390 *illustrating that the 35 fault segments at the seabed belong to 7 major faults (each fault*  
 391 *represented by one color). An example of some fault plane area measurements. (c-f) Structural*  
 392 *maps of four subsurface horizons (base units 4-1), each with faults crossing it (same colors as*  
 393 *in b). Note the hidden fault segment (dashed red line in a), which does not disrupt the seabed*  
 394 *but may rupture it in the future.*

395

396



397

398 *Figure 8: (a) Seabed faults in the Yam Hadera seismic survey with hidden fault segments*  
 399 *marked in the same colors as the fault to which it is connected in (b). (b) All faults are displacing*  
 400 *Base Unit 4. Each fault is represented by one color. (c) 3D illustration of 5 faults with their*  
 401 *measured fault plane area. Note that the yellow and the pink faults are not detected at the*  
 402 *seabed in some parts (hidden fault segments) despite their large plane area (101<sup>2</sup>, 37<sup>2</sup> km,*  
 403 *respectively), and their colors are the same as in (b).*

404

405

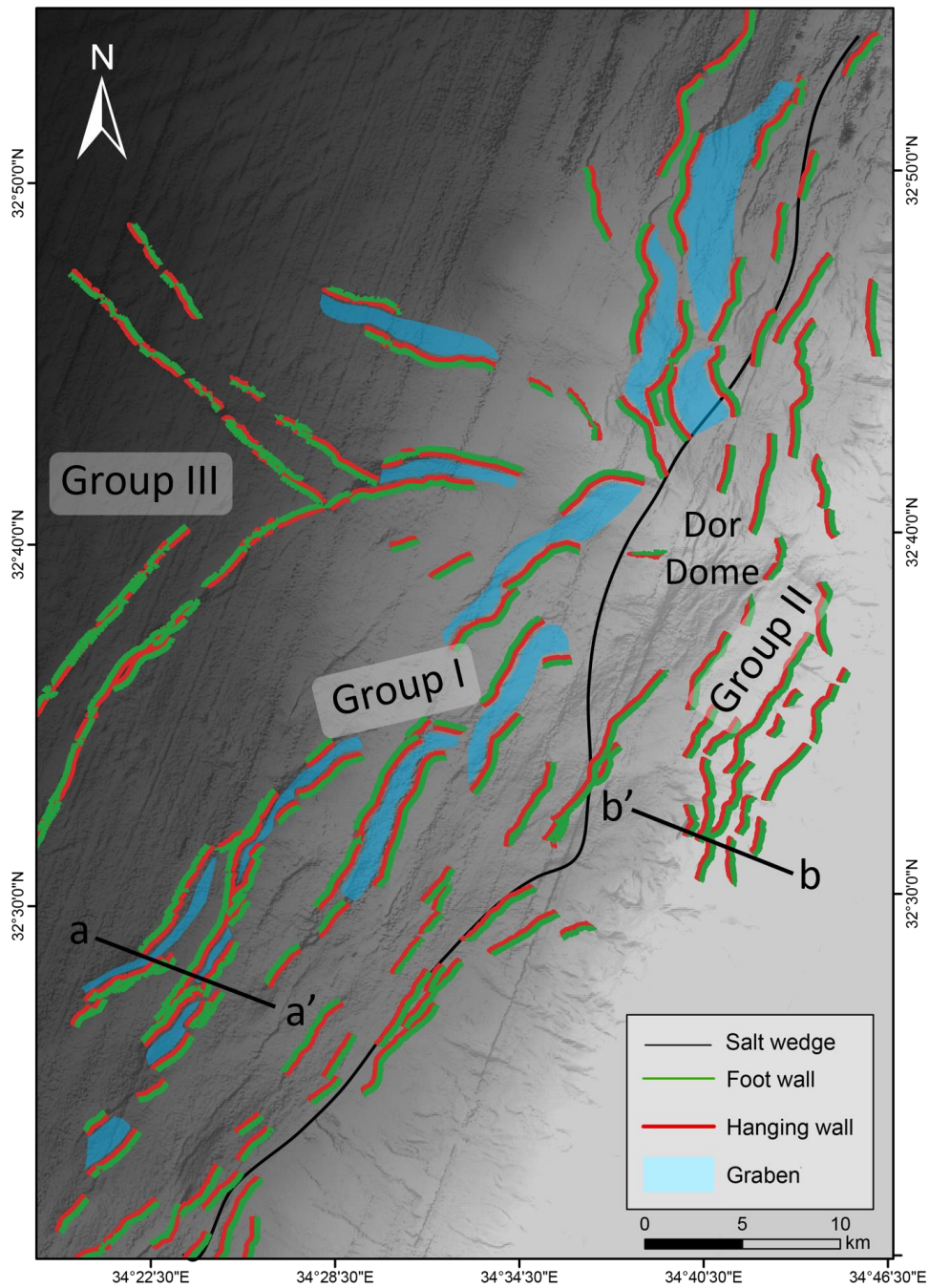
#### 4.2.3. *Geometry and location relative to the salt wedge*

406 Another way for fault classification is based on their geometry and location relative to  
407 the underlying salt layer (Fig. 9). Group I produce horsts and grabens (marked blue)  
408 mostly along the base of the continental slope, west of the salt wedge-out line. The  
409 faults of Group I displace the entire Pliocene–Quaternary section down to the top salt  
410 horizon (Fig. 10a, cross-section aa'), and their dip angle varies around  $45^{\circ}$  (Fig. 11).  
411

412 Group II consists of seaward dipping faults producing a series of down-stepping stairs  
413 (growth faults, rotated blocks, and half grabens) mainly in the upper slope, east of the  
414 salt wedge-out line (Fig. 9). These faults are highly listric (Fig. 10b, cross-section bb')  
415 as already described above (Fig. 5). They are characterized by smaller dip angles of  
416 about  $30^{\circ}$  (Fig. 11) and do not displace Unit 1 (Fig. 10b, cross-section bb').

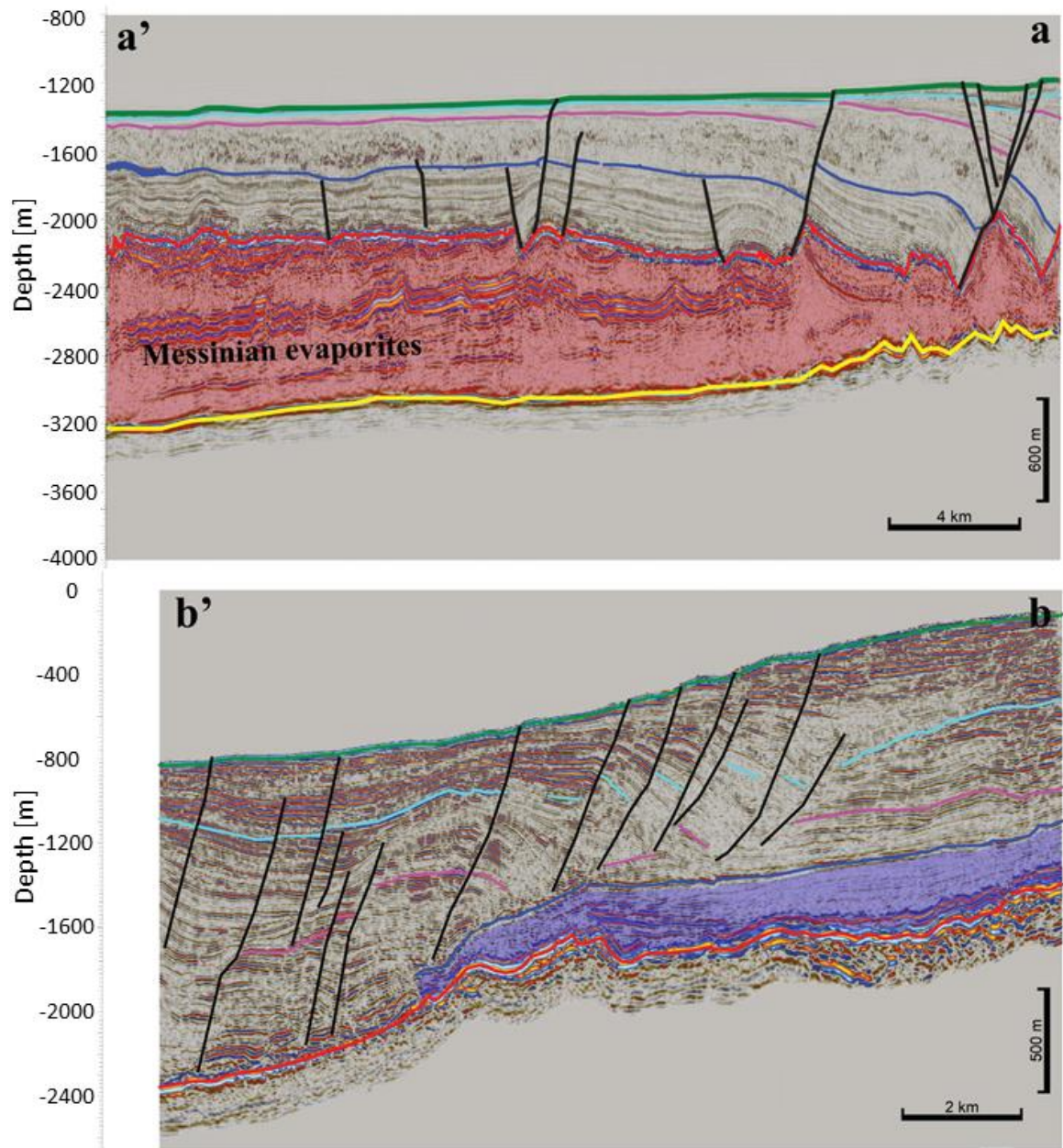
417 Group III are relatively long strike-slip faults with a few hundred meters of lateral  
418 displacement (Ben Zeev and Gvirtzman, 2020). Their vertical throw is relatively small,  
419 and its direction changes along the strike (Fig. 9).

420



421

422 *Figure 9: Classification of faults according to structure and location. The hanging wall in red,*  
 423 *the footwall in green, and the grabens in blue. Group I consists of horsts and grabens, running*  
 424 *along the base of the continental slope west of the salt wedge-out boundary (black line). Group*  
 425 *II consists of down-stepping normal faults with hanging walls always on the basinward side,*  
 426 *mostly located east of the salt wedge-out line. Group III is strike-slip faults. Bathymetry from*  
 427 *Tibor et al. (2013).*



428

429 *Figure 10: Seismic cross-sections illustrating the difference between Group I (a-a', Sara-Mira*  
 430 *survey) located west of the salt wedge and Group II (b-b', Yam-Hadera survey) located on the*  
 431 *continental slope east of the salt wedge (Messinian evaporites are missing). Note that the faults*  
 432 *of Group II do not displace the Top Unit 2 horizon (Unit 2 in blue). Location in Fig. 9.*

433

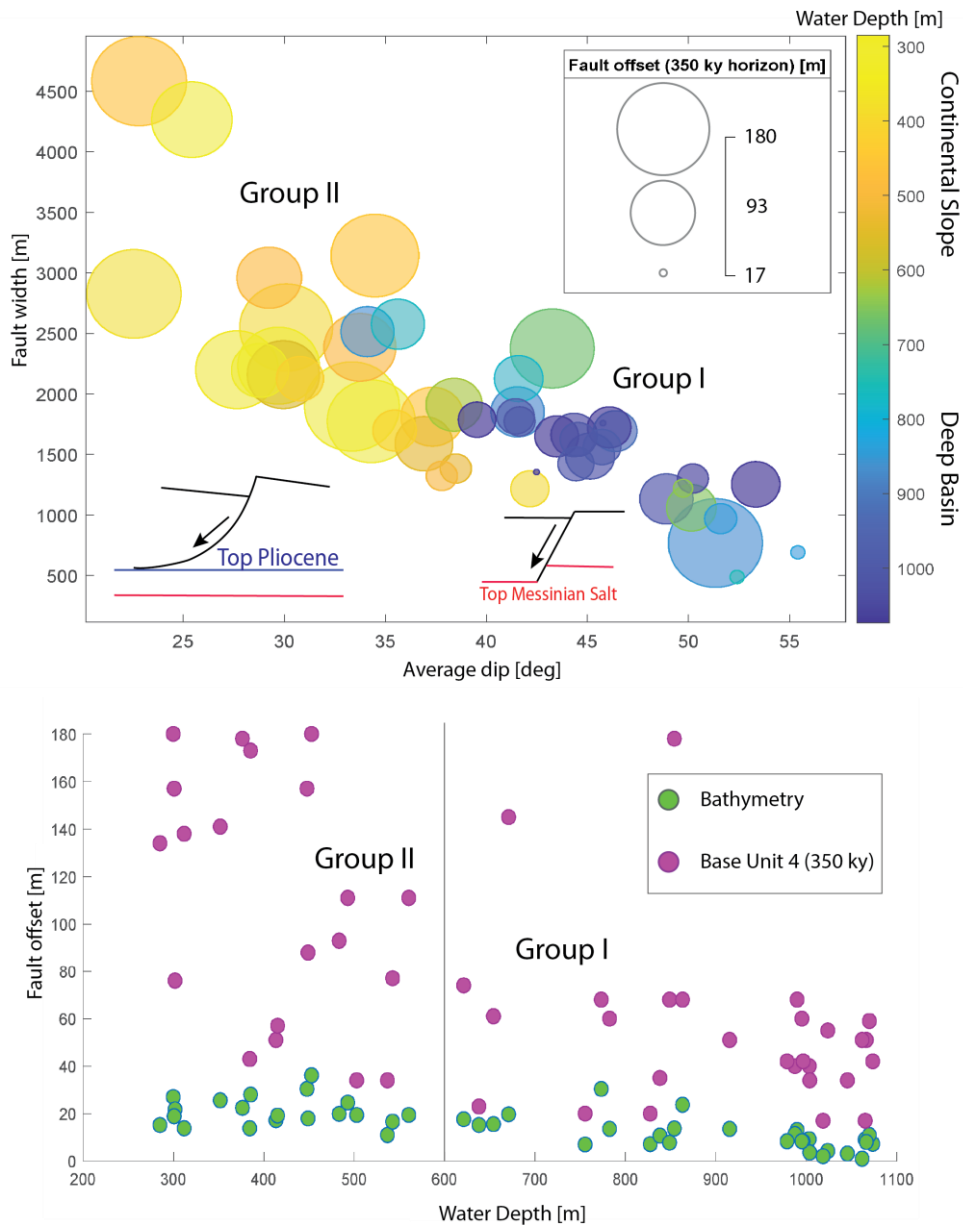
434 The high-resolution seismic volumes “Sara-Myra” and “Yam Hadera” allow detailed  
 435 investigation of the difference between Group I and Group II according to three  
 436 parameters: displacement (at the seabed and at the base Unit 4), fault plane dip, and  
 437 fault width. The upper panel in Fig. 11 illustrates that the fault width negatively

438 correlates with the dip angle (larger width for gently dipping faults). The lower panel  
439 of Fig. 11 further illustrates that displacement (seabed and base Unit 4) negatively  
440 correlates with water depth (faults in shallower waters have larger displacements).

441 Group I, located in the deeper waters (blue), is characterized by relatively small vertical  
442 offsets (better seen in the Base unit 4 horizon), high dip angles ( $>45^\circ$ ), and relatively  
443 short fault width (0.5-2 km). Group II (the listric faults), located in shallower waters  
444 (yellow), is characterized by larger (Base unit 4) vertical offsets, lower dip angles  
445 ( $\sim 30^\circ$ ), and larger faults widths (1.5-4.5 km). These observations highlight the listric  
446 faults (Group II), located east of the salt wedge-out line (Fig. 10b), which are big in size  
447 and in vertical offsets.

448

449



450

451 *Figure 11: Upper panel shows the relationship between the average faults dip angle; the fault*  
 452 *width; the location of the fault along the slope (water depth); and the offset of Base Unit 4*  
 453 *horizon. Group II, located on the upper slope, is characterized by larger fault width (1.5-4.5*  
 454 *km), gently dipping (~30°) fault planes and larger fault offsets. The lower panel shows the*  
 455 *difference between the offsets as they were measured on the seabed and Base Unit 4 (cumulative*  
 456 *offset). The differences in faults offsets are much larger in Group II.*

## 457 **5. Discussion**

### 458 *5.1. Seabed versus subsurface mapping of faults*

459 Detailed mapping of the seafloor has become standard practice in marine geohazard  
460 assessment, and the demand for improved resolution is continuously growing. Here we  
461 show that bathymetry is not enough for faults investigation, even if it is extremely  
462 detailed, because fault scarps are strongly affected by sedimentation and erosion; hence  
463 their heights do not represent the real offsets. In fact, the subsurface mapping may be  
464 more informative even if its resolution is lower. For example, peak vertical  
465 displacements of faults near the Dor disturbance are twice the size of those measured  
466 along nearby faults; yet this is not observed on the bathymetry because the scarps are  
467 quickly buried. Sedimentation rates averaged on 350 ky, indicate >200 cm/ky near the  
468 Dor disturbance (Fig. 4c). Moreover, a 6-m-long core retrieved nearby (location in Fig.  
469 4c) with sedimentation rate of >850 cm/ky (Ashkenazi et al., 2022), indicates that  
470 sedimentation rate may have increased in the last couple of thousands of years. Note  
471 that the sedimentation rates calculation includes all sources of material accumulated  
472 due to the downslope transport of materials.

473 The drawback of these measurements is their dependency on the quality of the seismic  
474 data. Where only 2D lines are available, the measured value represents the throws at  
475 the survey-fault intersection, which may represent the tip of the fault; moreover, some  
476 faults may not be crossed by any seismic profile.

477 Additional support for the advantage of subsurface mapping is the structural map of the  
478 350 ka horizon (Fig. 4b) and the calculated sedimentation rate map (Fig. 4c). These  
479 maps show that the most active regions in the study area are the half-grabens  
480 surrounding the Dor disturbance from the east (Fig. 5). These half-grabens are rapidly  
481 subsiding (thick Unit 4), and the faults bounding them are the most active. We suggest



482 that while the faults of Group I are driven by the salt flow that produces extension above  
483 it (Hamdani et al., 2021), the faults of Group II are also affected by the gravitational  
484 collapse of the continental slope.

#### 485 5.2. *Fault classification*

486 Based on the maximal displacement of base Unit 4 (Fig. 6c,d), we classify all fault  
487 segments mapped on the seabed (rupturing the seabed) to three vertical offset levels.  
488 Vertical offset smaller than 60 m is considered low; 60-100 m is considered moderate;  
489 and >100 m is considered high (Fig. 12a).

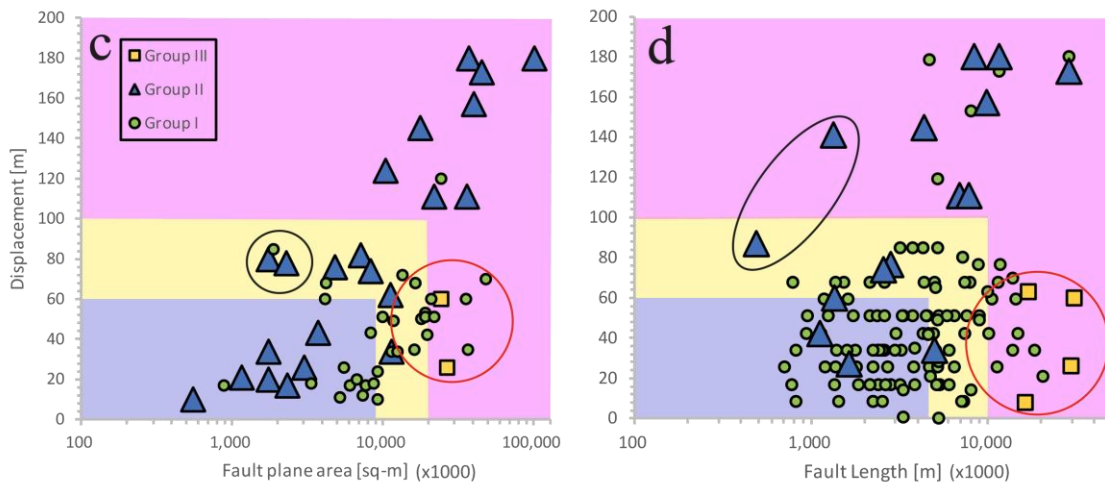
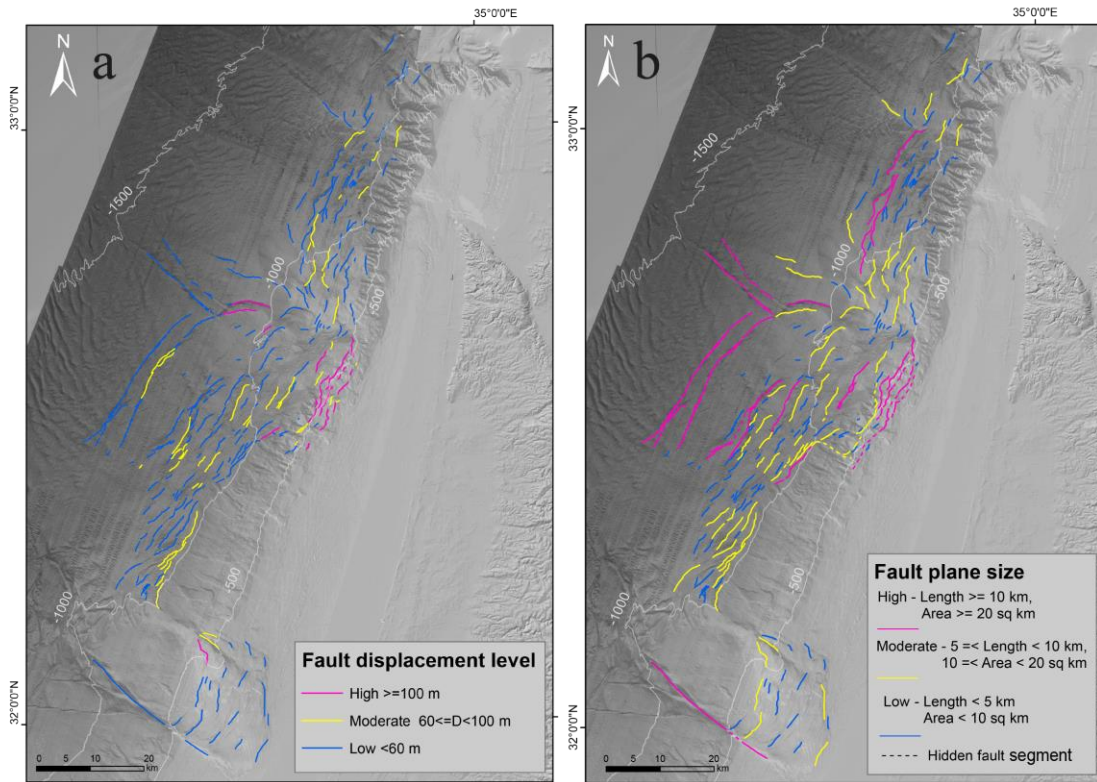
490 Based on the size (area of fault plane or its length on surface projection), we classify  
491 all faults mapped at the subsurface to three levels. Fault planes smaller than 10 km<sup>2</sup> or  
492 shorter than 5 km are considered small; an area of 10-20 km<sup>2</sup> or length of 5-10 km is  
493 considered moderate; and an area larger than 20 km<sup>2</sup> or length longer than 10 km is  
494 considered big (Fig. 12b).

495 It should be noted that unlike the classification by vertical displacement, which is  
496 performed on seabed segments, the classification of faults by size is performed on fault  
497 planes, and a single fault plain frequently combines many seabed segments (i.e., the  
498 number of fault planes in our database is significantly smaller than the number of seabed  
499 segments).

500 Though the two classification criteria are independently measured, and despite a certain  
501 degree of arbitrariness in choosing the cutoff values (60 m and 100 m of vertical  
502 displacement; 10 km<sup>2</sup> and 20 km<sup>2</sup> for fault plane area), it is interesting to compare the  
503 resulting maps. For most faults in the study area, the two criteria yield a similar category  
504 (Fig. 12c,d). That is, fault segments with high displacement levels are usually a part of  
505 a big fault and vice versa, similar to observations related to deep-seated tectonic faults  
506 (Wells and Coppersmith, 1994). Exceptions, marked in Fig. 12c,d by black circles

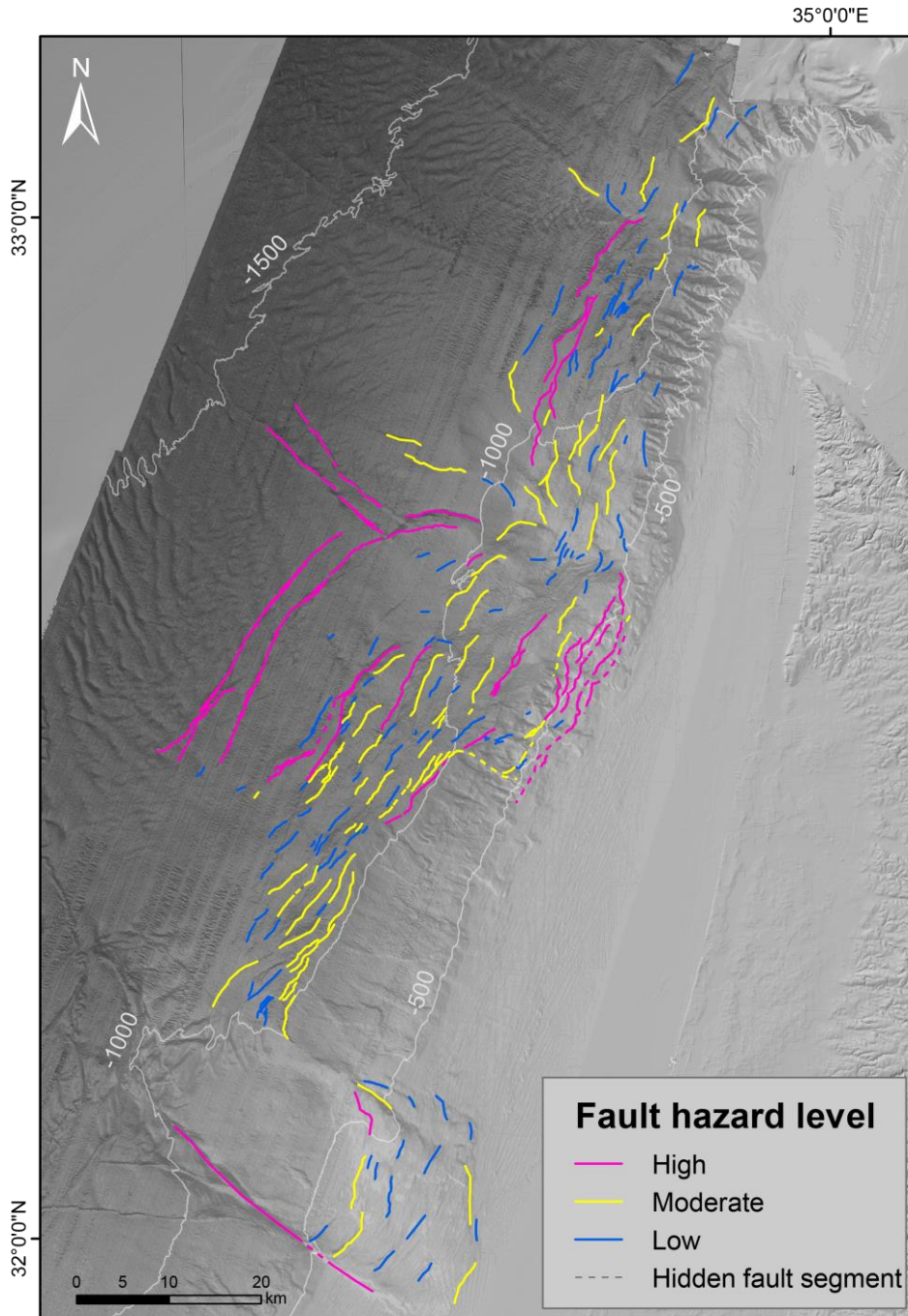
507 (moderate displacement and small faults), mainly belong to Group II, which is  
508 exceptional in many ways, as shown above. Conversely, exceptions marked by red  
509 circles (big faults with small displacement) belong to Group III, which are strike-slip  
510 faults whose vertical displacement is not expected to correlate with their dimensions.

511 Finally, we provide a simplified map that combines the two measured parameters to a  
512 single hazard level (Fig. 13). In this map, a high level is assigned to a fault segment,  
513 which either is characterized by high displacement or large planes; low means low  
514 displacement and small plane area; moderate is all the rest. This map simplifies the use  
515 of our analysis for early planning of new infrastructures on the seabed, which is the aim  
516 of this study.



518

519 *Figure 12: Fault classification by displacement (a) and size (b). Each seabed fault segment is*  
 520 *assigned a value based on its subsurface structure. i.e., the maximal displacement measured*  
 521 *along the fault segment at the base unit 4 horizon and the total area of all segments, connected*  
 522 *at the subsurface. When the 3D mapping of a fault is unavailable, fault size is expressed by its*  
 523 *length in a map view. (c,d) Displacement at base Unit 4 versus fault size (length/area). Pink,*  
 524 *yellow, and blue present three levels of displacement and size, which are proxies for surface*  
 525 *rupture and potential earthquake magnitudes, respectively. While classification by the two*  
 526 *criteria correlates for most faults, black circles mark faults whose displacement is high relative*  
 527 *to their size, and red circles mark faults that are big relative to their (vertical) displacement.*  
 528 *Bathymetry from Tibor et al. (2013).*



529

530 *Figure 13: Final simplified faults hazard map classified into three hazard levels according to*  
 531 *a combination of the two criteria presented in Fig. 12 (i.e., fault displacement and size). The*  
 532 *combination is conservative, i.e., a high level is assigned to a fault segment, which either is*  
 533 *characterized by high displacement or belongs to a big fault; low means low displacement and*  
 534 *small size; moderate are all the rest. Bathymetry from Tibor et al. (2013).*

535

536        5.3.    *Listric faults south of the Dor disturbance*

537    The listric faults south of the Dor disturbance (part of Group II) are particularly  
538    exceptional. Their planes dip gently with lower angles; they have a bigger width but do  
539    not penetrate Unit 1; they are located on the steep slope, east of the salt wedge; and  
540    particularly important, they produce large seabed scarps despite their location in a high  
541    sedimentation zone. In fact, the sedimentation rate at that location is four times larger  
542    than the displacement rate (~200 cm/ky vs. ~50 cm/ky, respectively. Fig. 3b, 4c).  
543    Allegedly, this observation indicates that these faults are creeping faster than the  
544    sedimentation rate, or they slip seismically, or they operate in rapid episodes of tremor  
545    and slip (ETS), or “slow earthquakes” (Ito and Obara, 2006; Ikari et al., 2011). The  
546    possibility of seismic rupture was already raised by Elfassi et al. (2019) for the deep  
547    basin faults of Group I in the Sara-Myra survey, where sedimentation rates are similar  
548    or slightly higher than displacement rates. In that case, continuous creep seems unlikely  
549    because its rate is similar to the burial rate and cannot produce significant seabed scarps.

550        5.4.    *Earthquakes and faults*

551    If the thin-skinned faults offshore Israel are seismically active, they might produce  
552    earthquakes and ground shaking in addition to surface rupture. This possibility is  
553    apparently supported by the many epicenters located near the faults and particularly  
554    around the Dor Disturbance (Wetzler and Kurzon, 2016). The problem is that the depths  
555    of these earthquakes are much deeper (10-30 km) than the shallow thin-skinned faults  
556    (1-2 km). Katz and Hamiel, (2019) argued that many hypocenters coincide with the  
557    CMFZ at a depth of about 18 km, but this is inconsistent with Gvirtzman and Steinberg,  
558    (2012), who showed that the CMFZ stopped operating in the Miocene.

559    The accuracy of hypocenters depths offshore Israel is highly uncertain, as stated by  
560    Wetzler and Kurzon (2016), because of the lack of seismic stations at sea and because

561 of the simplified velocity model they extended from the onshore area. Therefore, at this  
562 stage, we cannot determine whether the recorded earthquakes offshore Israel are  
563 produced by thin-skinned faults or by deeper sources.

564 Another source of uncertainty is the area of the measured fault planes, which commonly  
565 exceeds 10 km<sup>2</sup> and even 20 km<sup>2</sup> (Fig. 8, 12b), while the earthquake magnitudes are  
566 mostly 2<M<4 (Wetzler and Kurzon, 2016). These values are inconsistent with the  
567 empiric relations measured in deep-seated faults (Wells and Coppersmith, 1994), where  
568 fault planes of 10-20 km<sup>2</sup> are typically associated with M~5 earthquakes. However,  
569 deep-seated faults are different from thin-skinned faults in many ways leaving us with  
570 unclerness. This short discussion indicates that the seismicity of the thin-skinned faults  
571 needs more research, which is crucial for hazard assessment. At this stage, we cannot  
572 tell if the thin-skinned faults creep very fast, rupture seismically or produce episodes  
573 tremor and slip (ETS).

## 574 **6. Summary and conclusions**

- 575 1. The need for geohazard assessment in the marine environment is increasing  
576 globally. Yet, in the field of hazard maps for planning and building, the offshore  
577 regions are commonly lagging decades behind the onshore practice.
- 578 2. Mapping 'active' faults in the marine environment is particularly complicated. If  
579 the onshore practice is followed, a Holocene horizon needs to be detected in the  
580 subsurface; then, for each fault, the question whether this horizon is displaced or  
581 not needs to be answered. This requires high-resolution seismic surveys and  
582 numerous coring and thus cannot be done for large regions.
- 583 3. In site-specific surveys, detailed bathymetry has become the main tool for mapping  
584 faults. Yet, we demonstrate that this is insufficient because fault scarps are

585 decreased by sedimentation and erosion, particularly in sediment-rich environments  
586 such as continental margins.

587 4. Here, we take advantage of the marine environment (wealth of seismic data) to  
588 produce maps that cannot be produced onshore. First, we map a subsurface horizon  
589 dated to 350 ka in the entire study area. Second, we measure vertical fault  
590 displacements along this horizon. Third, we map fault planes combining several  
591 fault segments and measure their size.

592 5. By classifying all faults according to their vertical displacement and size, we  
593 prepare two hazard maps, which are further combined into a single simplified fault  
594 hazard map.

595 6. Our maps are particularly useful for master planning. The sedimentation rates map  
596 alone immediately reveals tectonically active grabens, and the hazard maps help  
597 define the most hazardous zones.

598 7. Using our maps, we revealed a particularly problematic zone in the upper slope  
599 south of the Dor disturbance. In this area, a series of big listric faults are  
600 characterized by large displacements. The sedimentation rate in this location is also  
601 exceptional - four times faster than the displacement rate - and still, fault scarps are  
602 prominent. We suggest that this indicates rapid creep, seismic rupture, or episodic  
603 motions.

## 604 **7. Author contribution**

605 This study was conceptualized by ML under the supervision of ZG. Formal analysis,  
606 visualization of results and writing of the original draft were performed by ML. All  
607 authors contributed to the interpretation of the findings and revision of the paper.

608

## 609 **8. Competing interests**

610 The authors declare that they have no conflict of interest.

## 611 **9. Data availability**

612 The seismic datasets related to this article are industrial data from the Geological Survey of  
613 Israel. Details can be obtained from the Israel Ministry of Energy  
614 (<https://prime.energy.gov.il/>). Please contact the author via email for more details regarding  
615 the fault scarps algorithm, maps, and layers.

## 616 **10. Acknowledgments**

617

618 We are grateful to Delek Ltd. and Modiin Energy (Israel) for their permission to release  
619 data. We thank HIS Markit (London, UK) for providing the Kingdom academic licenses  
620 for seismic interpretation. Thanks to our colleagues in the subsurface laboratory at the  
621 Geological Survey of Israel. This research was funded by the Israeli Ministry of Energy,  
622 and the National Committee of Earthquake Preparedness and Mitigation. We also  
623 heartily thank the editor Maria Ana Baptista, reviewer Stéphane Baize, and an  
624 anonymous reviewer, for their constructive and important comments to improve the  
625 quality of this paper.



## 626 **11.References**

- 627 Allen, H., Jackson, C. A. L., and Fraser, A. J.: Gravity-driven deformation of a  
628 youthful saline giant: The interplay between gliding and spreading in the Messinian  
629 basins of the Eastern Mediterranean, *Pet. Geosci.*, 22, 340–356,  
630 <https://doi.org/10.1144/petgeo2016-034>, 2016.
- 631 Almagor, G.: Salt-controlled slumping on the Mediterranean slope of central Israel,  
632 *Mar. Geophys. Res.*, 6, 227–243, <https://doi.org/10.1007/BF00286527>, 1984.
- 633 Almagor, G. and Garfunkel, Z.: Submarine Slumping in Continental Margin of Israel  
634 and Northern Sinai., *AAPG Bull*, 63, 324–340, [https://doi.org/10.1306/c1ea5607-](https://doi.org/10.1306/c1ea5607-16c9-11d7-8645000102c1865d)  
635 [16c9-11d7-8645000102c1865d](https://doi.org/10.1306/c1ea5607-16c9-11d7-8645000102c1865d), 1979.
- 636 Almagor, G. and Hall, J. K.: Morphology of the continental margin off NE Sinai and  
637 southern Israel., *Isr. J. Earth Sci.*, 27, 128–132, 1979.
- 638 Angell, M. M., Geophysics, A. O. A., Hanson, K., Youngs, R., and Abramson, H.:  
639 Probabilistic fault displacement hazard assessment for flowlines and export pipelines,  
640 mad dog and Atlantis field developments, deepwater Gulf of Mexico, *Proc. Annu.*  
641 *Offshore Technol. Conf.*, 2003-May, 2579–2603, <https://doi.org/10.4043/15402-ms>,  
642 2003.
- 643 Armijo, R., Pondard, N., Meyer, B., Uçarkus, G., De Lépinay, B. M., Malavieille, J.,  
644 Dominguez, S., Gustcher, M. A., Schmidt, S., Beck, C., Cagatay, N., Cakir, Z., Imren,  
645 C., Eris, K., Natalin, B., Özalaybey, S., Tolun, L., Lefèvre, I., Seeber, L., Gasperini,  
646 L., Rangin, C., Emre, O., and Sarikavak, K.: Submarine fault scarps in the Sea of  
647 Marmara pull-apart (North Anatolian Fault): Implications for seismic hazard in  
648 Istanbul, *Geochemistry, Geophys. Geosystems*, 6, 1–29,  
649 <https://doi.org/10.1029/2004GC000896>, 2005.
- 650 Ashkenazi, L., Katz, O., Abramovich, S., Almogi-Labin, A., Makovsky, Y., Gadol,  
651 O., Kanari, M., Masque, P., and Hyams-Kaphzan, O.: Benthic foraminifera as  
652 indicators of recent mixed turbidite-contourite sediment transport system in the  
653 Eastern Mediterranean upper continental slope, offshore Israel, *Mar. Geol.*, 445,  
654 106756, <https://doi.org/10.1016/j.margeo.2022.106756>, 2022.
- 655 Avni, Y., Segev, A., and Ginat, H.: Oligocene regional denudation of the northern

656 Afar dome: Pre- and syn-breakup stages of the Afro-Arabian plate, *Bull. Geol. Soc.*  
657 *Am.*, 124, 1871–1897, <https://doi.org/10.1130/B30634.1>, 2012.

658 Bar, O., Gvirtzman, Z., Feinstein, S., and Zilberman, E.: Accelerated subsidence and  
659 sedimentation in the Levant Basin during the Late Tertiary and concurrent uplift of  
660 the Arabian platform: Tectonic versus counteracting sedimentary loading effects,  
661 *Tectonics*, 32, 334–350, <https://doi.org/10.1002/TECT.20026>, 2013.

662 Bar, O., Zilberman, E., Feinstein, S., Calvo, R., and Gvirtzman, Z.: The uplift history  
663 of the Arabian Plateau as inferred from geomorphologic analysis of its northwestern  
664 edge, *Tectonophysics*, 671, 9–23, <https://doi.org/10.1016/J.TECTO.2016.01.004>,  
665 2016.

666 Barrie, J. V., Hill, P. R., Conway, W., Iwanowska, K., and Picard, K.: Environmental  
667 Marine Geoscience 4. Georgia Basin: Seabed Features and Marine Geohazards, 32,  
668 2005.

669 Bein, A. and Gvirtzman, G.: A Mesozoic fossil edge of the Arabian Plate along the  
670 Levant coastline and its bearing on the evolution of the Eastern Mediterranean, *Struct.*  
671 *Hist. Mediterr. Basins. 25th Congr. Int. Comm. Sci. Explor. Mediterr. Sea. Split.*  
672 *Yugosl.*, 95–109, 1977.

673 Ben-Avraham, Z.: The structure and tectonic setting of the levant continental margin,  
674 Eastern Mediterranean, *Tectonophysics*, 46, 313–331, [https://doi.org/10.1016/0040-1951\(78\)90210-X](https://doi.org/10.1016/0040-1951(78)90210-X), 1978.

675

676 Ben-Gai, Y., Ben-Avraham, Z., Buchbinder, B., and Kendall, C. G. S. C.: Post-  
677 Messinian evolution of the Southeastern Levant Basin based on two-dimensional  
678 stratigraphic simulation, *Mar. Geol.*, 221, 359–379,  
679 <https://doi.org/10.1016/j.margeo.2005.03.003>, 2005.

680 Ben Zeev, Y. and Gvirtzman, Z.: When Two Salt Tectonics Systems Meet: Gliding  
681 Downslope the Levant Margin and Salt Out-Squeezing From Under the Nile Delta,  
682 *Tectonics*, 1–24, <https://doi.org/10.1029/2019tc005715>, 2020.

683 Bertoni, C. and Cartwright, J.: Messinian evaporites and fluid flow, *Mar. Pet. Geol.*,  
684 66, 165–176, <https://doi.org/10.1016/J.MARPETGEO.2015.02.003>, 2015.

685 Bertoni, C. and Cartwright, J. A.: 3D seismic analysis of circular evaporite dissolution

686 structures, Eastern Mediterranean, *J. Geol. Soc. London.*, 162, 909–926,  
687 <https://doi.org/10.1144/0016-764904-126>, 2005.

688 Bertoni, C. and Cartwright, J. A.: Controls on the basinwide architecture of late  
689 Miocene (Messinian) evaporites on the Levant margin (Eastern Mediterranean),  
690 *Sediment. Geol.*, 188–189, 93–114, <https://doi.org/10.1016/J.SEDGEO.2006.03.019>,  
691 2006.

692 Bertoni, C. and Cartwright, J. A.: Major erosion at the end of the Messinian Salinity  
693 Crisis: Evidence from the Levant Basin, Eastern Mediterranean, *Basin Res.*, 19, 1–18,  
694 <https://doi.org/10.1111/j.1365-2117.2006.00309.x>, 2007.

695 Bryant, W. A. and Hart, E. W.: Fault-rupture hazard zones in California, *Spec. Publ.*,  
696 42, 2–7, 2007.

697 Buchbinder, B. and Zilberman, E.: Sequence stratigraphy of Miocene - Pliocene  
698 carbonate - Siliciclastic shelf deposits in the eastern Mediterranean margin (Israel):  
699 Effects of eustasy and tectonics, *Sediment. Geol.*, 112, 7–32,  
700 [https://doi.org/10.1016/S0037-0738\(97\)00034-1](https://doi.org/10.1016/S0037-0738(97)00034-1), 1997.

701 Buchbinder, B., Martinotti, G. M., Siman-Tov, R., and Zilberman, E.: Temporal and  
702 spatial relationships in Miocene reef carbonates in Israel, *Palaeogeogr.*  
703 *Palaeoclimatol. Palaeoecol.*, 101, 97–116, [https://doi.org/10.1016/0031-](https://doi.org/10.1016/0031-0182(93)90154-B)  
704 0182(93)90154-B, 1993.

705 C. H. Bruce: Pressured Shale and Related Sediment Deformation--Mechanism for  
706 Development of Regional Contemporaneous Faults: ABSTRACT, *Am. Assoc. Pet.*  
707 *Geol. Bull.*, 57, 878–886, [https://doi.org/10.1306/83d91213-16c7-11d7-](https://doi.org/10.1306/83d91213-16c7-11d7-8645000102c1865d)  
708 8645000102c1865d, 1973.

709 Carmel, Z., Inman, D. L., and Golik, A.: Directional wave measurement at Haifa,  
710 Israel, and sediment transport along the Nile littoral cell, *Coast. Eng.*, 9, 21–36,  
711 [https://doi.org/10.1016/0378-3839\(85\)90025-0](https://doi.org/10.1016/0378-3839(85)90025-0), 1985.

712 Cartwright, J., Jackson, M., Dooley, T., and Higgins, S.: Strain partitioning in gravity-  
713 driven shortening of a thick, multilayered evaporite sequence, *Geol. Soc. Spec. Publ.*,  
714 363, 449–470, <https://doi.org/10.1144/SP363.21>, 2012.

715 Cartwright, J., Kirkham, C., Bertoni, C., Hodgson, N., and Rodriguez, K.: Direct

716 calibration of salt sheet kinematics during gravity-driven deformation, *Geology*, 46,  
717 623–626, <https://doi.org/10.1130/G40219.1>, 2018.

718 Cartwright, J. A. and Jackson, M. P. A.: Initiation of gravitational collapse of an  
719 evaporite basin margin: The Messinian saline giant, Levant Basin, eastern  
720 Mediterranean, *Bull. Geol. Soc. Am.*, 120, 399–413,  
721 <https://doi.org/10.1130/B26081X.1>, 2008.

722 Chiocci, F. L. and Ridente, D.: Regional-scale seafloor mapping and geohazard  
723 assessment. The experience from the Italian project MaGIC (Marine Geohazards  
724 along the Italian Coasts), *Mar. Geophys. Res.*, 32, 13–23,  
725 <https://doi.org/10.1007/s11001-011-9120-6>, 2011.

726 Clark, I. R. and Cartwright, J. A.: Interactions between submarine channel systems  
727 and deformation in deepwater fold belts: Examples from the Levant Basin, Eastern  
728 Mediterranean sea, *Mar. Pet. Geol.*, 26, 1465–1482,  
729 <https://doi.org/10.1016/j.marpetgeo.2009.05.004>, 2009.

730 Clark, S. H., Field, M. E., and Hirozawa, C. A.: Reconnaissance geology and geologic  
731 hazards of the offshore Coos Bay basin, Oregon., *US Geol. Surv. Bull.*, 1645, 1985.

732 Cornell, C. A.: ENGINEERING SEISMIC RISK ANALYSIS, *Bulletin of the*  
733 *Seismological Society of America*, 1583–1606 pp., 1968.

734 Cornell, C. A.: Probabilistic analysis of damage to structures under seismic loads,  
735 *Dyn. Waves Civ. Eng. Proc. a Conf. Organised by Soc. Earthq. Civ. Eng. Dyn.*, 473–  
736 493, 1971.

737 Crans, W., Mandl, G., and Haremboure, J.: on the Theory of Growth Faulting: a  
738 Geomechanical Delta Model Based on Gravity Sliding, *J. Pet. Geol.*, 2, 265–307,  
739 <https://doi.org/10.1111/j.1747-5457.1980.tb00707.x>, 1980.

740 De-Sitter, L. U.: Structural development of the Arabian Shield in Palestine, *Geol. en*  
741 *Mijnb.*, 41, 116–124, 1962.

742 Elfassi, Y., Gvirtzman, Z., Katz, O., and Aharonov, E.: Chronology of post-Messinian  
743 faulting along the Levant continental margin and its implications for salt tectonics,  
744 *Mar. Pet. Geol.*, 109, 574–588, <https://doi.org/10.1016/j.marpetgeo.2019.05.032>,  
745 2019.

746 Elias, A., Tapponnier, P., Singh, S. C., King, G. C. P., Briais, A., Daëron, M., Carton,  
747 H., Sursock, A., Jacques, E., Jomaa, R., and Klinger, Y.: Active thrusting offshore  
748 Mount Lebanon: Source of the tsunamigenic A.D. 551 Beirut-Tripoli earthquake,  
749 *Geology*, 35, 755–758, <https://doi.org/10.1130/G23631A.1>, 2007.

750 Evamy, B. D., Haremboure, J., Kamerling, P., Knaap, W. A., Molloy, F. A., and  
751 Rowlands, P. H.: Hydrocarbon Habitat of Tertiary Niger Delta, *Am. Assoc. Pet. Geol.*  
752 *Bull.*, 62, 1–39, <https://doi.org/10.1306/C1EA47ED-16C9-11D7>  
753 8645000102C1865D, 1978.

754 Eyal, Y. and Reches, Z.: Tectonic analysis of the Dead Sea Rift Region since the  
755 Late-Cretaceous based on mesostructures, *Tectonics*, 2, 167–185,  
756 <https://doi.org/10.1029/TC002i002p00167>, 1983.

757 Freund, R.: The Triassic-Jurassic structure of Israel and its relation to the origin of the  
758 eastern Mediterranean, 1975.

759 Gadol, O., Tibor, G., ten Brink, U., Hall, J. K., Groves-Gidney, G., Bar-Am, G.,  
760 Hübscher, C., and Makovsky, Y.: Semi-automated bathymetric spectral  
761 decomposition delineates the impact of mass wasting on the morphological evolution  
762 of the continental slope, offshore Israel, *Basin Res.*, bre.12420,  
763 <https://doi.org/10.1111/bre.12420>, 2019.

764 Garfunkel, Z., Arad, A., and Almagor, G.: Palmahim disturbance and similar  
765 structures offshore Israel, Israel Electric Corp, 1977.

766 Garfunkel, Z.: Large-scale submarine rotational slumps and growth faults in the  
767 Eastern Mediterranean, *Mar. Geol.*, 55, 305–324, <https://doi.org/10.1016/0025->  
768 3227(84)90074-4, 1984.

769 Garfunkel, Z.: The pre-Quaternary geology of Israel, *zoogeography Isr.*, 7–34, 1988.

770 Garfunkel, Z.: Constrains on the origin and history of the Eastern Mediterranean  
771 basin, *Tectonophysics*, 298, 5–35, [https://doi.org/10.1016/S0040-1951\(98\)00176-0](https://doi.org/10.1016/S0040-1951(98)00176-0),  
772 1998.

773 Garfunkel, Z. and Almagor, G.: Geology and structure of the continental margin off  
774 northern Israel and the adjacent part of the Levantine Basin, *Mar. Geol.*, 62, 105–131,  
775 [https://doi.org/10.1016/0025-3227\(84\)90057-4](https://doi.org/10.1016/0025-3227(84)90057-4), 1984.

776 Garfunkel, Z. and Derin, B.: Permian-early Mesozoic tectonism and continental  
777 margin formation in Israel and its implications for the history of the Eastern  
778 Mediterranean, *Geol. Soc. Spec. Publ.*, 17, 187–201,  
779 <https://doi.org/10.1144/GSL.SP.1984.017.01.12>, 1984.

780 Garfunkel, Z., Almagor, G., and Arad, A.: The Palmahim disturbance and its regional  
781 setting, *Geol. Surv. Isr. Bull.*, 72, 1–58, 1979.

782 Ginzburg, A., Ben-Avraham, Z.: The deep structure of the central and southern  
783 Levant continental margin. *Ann. Tectonicae* 1, 105–115, 1987.

784 Goldsmith, V. and Golik, A.: Sediment transport model of the southeastern  
785 Mediterranean coast, *Mar. Geol.*, 37, 147–175, [https://doi.org/10.1016/0025-](https://doi.org/10.1016/0025-3227(80)90015-8)  
786 [3227\(80\)90015-8](https://doi.org/10.1016/0025-3227(80)90015-8), 1980.

787 Golik, A.: Indirect evidence for sediment transport on the continental shelf off Israel,  
788 *Geo-Marine Lett.*, 13, 159–164, <https://doi.org/10.1007/BF01593189>, 1993.

789 Golik, A.: Pattern of sand transport along the Israeli coastline, *Isr. J. Earth Sci.*, 51,  
790 191–202, <https://doi.org/10.1560/3K9B-6GX6-J9XJ-LCLM>, 2002.

791 Gradmann, S., Hübscher, C., Ben-Avraham, Z., Gajewski, D., and Netzeband, G.: Salt  
792 tectonics off northern Israel, *Mar. Pet. Geol.*, 22, 597–611,  
793 <https://doi.org/10.1016/j.marpetgeo.2005.02.001>, 2005.

794 Gvirtzman, G. and Buchbinder, B.: Recent and Pleistocene coral reefs and coastal  
795 sediments of the Gulf of Elat, *Guideb. 10th Int. Congr. Sedimentol.*, 162–191, 1978.

796 Gvirtzman, Z. and Garfunkel, Z.: Vertical movements following intracontinental  
797 magmatism: An example from southern Israel, *J. Geophys. Res. Solid Earth*, 102,  
798 2645–2658, <https://doi.org/10.1029/96jb02567>, 1997.

799 Gvirtzman, Z. and Garfunkel, Z.: The transformation of southern Israel from a swell  
800 to a basin: Stratigraphic and geodynamic implications for intracontinental tectonics,  
801 *Earth Planet. Sci. Lett.*, 163, 275–290, [https://doi.org/10.1016/S0012-821X\(98\)00193-](https://doi.org/10.1016/S0012-821X(98)00193-9)  
802 [9](https://doi.org/10.1016/S0012-821X(98)00193-9), 1998.

803 Gvirtzman, Z. and Steinberg, J.: Inland jump of the Arabian northwest plate boundary  
804 from the Levant continental margin to the Dead Sea Transform, *Tectonics*, 31,  
805 <https://doi.org/10.1029/2011TC002994>, 2012.

806 Gvirtzman, Z., Zilberman, E., and Folkman, Y.: Reactivation of the Levant passive  
807 margin during the late Tertiary and formation of the Jaffa Basin offshore central  
808 Israel, *165*, 563–578, 2008.

809 Gvirtzman, Z., Reshef, M., Buch-Leviatan, O., and Ben-Avraham, Z.: Intense salt  
810 deformation in the Levant Basin in the middle of the Messinian Salinity Crisis, *Earth*  
811 *Planet. Sci. Lett.*, *379*, 108–119, <https://doi.org/10.1016/J.EPSL.2013.07.018>, 2013.

812 Gvirtzman, Z., Reshef, M., Buch-Leviatan, O., Groves-Gidney, G., Karcz, Z.,  
813 Makovsky, Y., and Ben-Avraham, Z.: Bathymetry of the Levant basin: interaction of  
814 salt-tectonics and surficial mass movements, *Mar. Geol.*, *360*, 25–39,  
815 <https://doi.org/10.1016/J.MARGE.2014.12.001>, 2015.

816 Gvirtzman, Z., Manzi, V., Calvo, R., Gavrieli, I., Gennari, R., Lugli, S., Reghizzi, M.,  
817 and Roveri, M.: Intra-Messinian truncation surface in the Levant Basin explained by  
818 subaqueous dissolution, *Geology*, *45*, 915–918, <https://doi.org/10.1130/G39113.1>,  
819 2017.

820 Hamdani, I., Aharonov, E., Olive, J. A., Perez, S., and Gvirtzman, Z.: Initiating Salt  
821 Tectonics by Tilting: Viscous Coupling Between a Tilted Salt Layer and Overlying  
822 Brittle Sediment, *J. Geophys. Res. Solid Earth*, *126*,  
823 <https://doi.org/10.1029/2020JB021503>, 2021.

824 Harding, T. P. and Lowell, J. D.: Structural Styles, Their Plate-Tectonic Habitats, and  
825 Hydrocarbon Traps in Petroleum Provinces, *Am. Assoc. Pet. Geol. Bull.*, *63*, 1016–  
826 1058, <https://doi.org/10.1306/2F9184B4-16CE-11D7-8645000102C1865D>, 1979.

827 Henson, R. S.: Observations on the Geology and Petroleum Occurrences in the  
828 Middle East, 1951.

829 Hough, G., Green, J., Fish, P., Mills, A., and Moore, R.: A geomorphological  
830 mapping approach for the assessment of seabed geohazards and risk, *Mar. Geophys.*  
831 *Res.*, *32*, 151–162, <https://doi.org/10.1007/s11001-010-9111-z>, 2011.

832 Hsü, K., Cita, M. B., and Ryan, W.: The origin of the Mediterranean evaporites,  
833 *Initial Reports Deep Sea Drill. Proj. 13*, Part 2,  
834 <https://doi.org/10.2973/dsdp.proc.13.143.1973>, 1973.

835 Hubscher, C., Beitz, M., Dummong, S., Gradmann, S., Meier, K., and Netzband, G.:

836 Stratigraphy, fluid dynamics and structural evolution of the Messinian Evaporites in  
837 the Levant Basin, eastern Mediterranean Sea, The Messinian Salinity Crisis from  
838 Mega-Deposits to Microbiology - A Consensus Report, 168 pp., 2008.

839 Hübscher, C. and Netzeband, G.: Evolution of a young salt giant:: The example of the  
840 Messinian evaporites in the Levantine Basin, 2007.

841 Ikari, M. J., Saffer, D. M., Editors, G., Saffer, D., Henry, P., and Tobin, H.:  
842 Comparison of frictional strength and velocity dependence between fault zones in the  
843 Nankai accretionary complex, *Geochemistry, Geophys. Geosystems*, 12, 0–11,  
844 <https://doi.org/10.1029/2010GC003442>, 2011.

845 Ito, Y. and Obara, K.: Very low frequency earthquakes within accretionary prisms are  
846 very low stress-drop earthquakes, *Geophys. Res. Lett.*, 33,  
847 <https://doi.org/10.1029/2006GL025883>, 2006.

848 Kafri, U. and Folkman, Y.: Multiphase reverse vertical tectonic displacement across  
849 major faults in northern Israel, *Earth Planet. Sci. Lett.*, 53, 343–348,  
850 [https://doi.org/10.1016/0012-821X\(81\)90039-X](https://doi.org/10.1016/0012-821X(81)90039-X), 1981.

851 Kanari, M., Tibor, G., Hall, J. K., Ketter, T., Lang, G., and Schattner, U.: Sediment  
852 transport mechanisms revealed by quantitative analyses of seafloor morphology: New  
853 evidence from multibeam bathymetry of the Israel exclusive economic zone, *Mar. Pet.  
854 Geol.*, 114, 104224, <https://doi.org/10.1016/J.MARPETGEO.2020.104224>, 2020.

855 Katz, O. and Hamiel, Y.: The nature of small to medium earthquakes along the  
856 Eastern Mediterranean passive continental margins, and their possible relationships to  
857 landslides and submarine salt-tectonic-related shallow faults, *Geol. Soc. London,  
858 Spec. Publ.*, 477, 15–22, <https://doi.org/10.1144/sp477.5>, 2019.

859 Katz, O., Reuven, E., and Aharonov, E.: Submarine landslides and fault scarps along  
860 the eastern Mediterranean Israeli continental-slope, *Mar. Geol.*, 369, 100–115,  
861 <https://doi.org/10.1016/j.margeo.2015.08.006>, 2015.

862 Kirkham, C., Cartwright, J., Bertoni, C., Rodriguez, K., and Hodgson, N.: 3D  
863 kinematics of a thick salt layer during gravity-driven deformation, *Mar. Pet. Geol.*,  
864 110, 434–449, <https://doi.org/10.1016/J.MARPETGEO.2019.07.036>, 2019.

865 Kingdom IHS Markit: <https://ihsmarkit.com/index.html>, 2022.



866 Klein, M., Zviely, D., Kit, E., and Shteinman, B.: Sediment Transport along the Coast  
867 of Israel: Examination of Fluorescent Sand Tracers, *J. Coast. Res.*, 236, 1462–1470,  
868 <https://doi.org/10.2112/05-0488.1>, 2007.

869 Krenkel, E.: Die Bruchzonen Ostafrikas, *Geol. Rundschau*, 14, 209–232,  
870 <https://doi.org/10.1007/BF01810069>, 1924.

871 Kvalstad, T. J.: What is the Current “Best Practice” in Offshore Geohazard  
872 Investigations? A State-of-the-Art Review, <https://doi.org/10.4043/18545-ms>, 2007.

873 Loncke, L., Gaullier, V., Mascle, J., Vendeville, B., and Camera, L.: The Nile deep-  
874 sea fan: An example of interacting sedimentation, salt tectonics, and inherited subsalt  
875 paleotopographic features, *Mar. Pet. Geol.*, 23, 297–315,  
876 <https://doi.org/10.1016/j.marpetgeo.2006.01.001>, 2006.

877 Mart, Y. and Gai, Y. B.: Some depositional patterns at continental margin of  
878 southeastern Mediterranean Sea., *Am. Assoc. Pet. Geol. Bull.*,  
879 <https://doi.org/10.1306/03B59B39-16D1-11D7-8645000102C1865D>, 1982.

880 Mart, Y. and Ryan, W.: The levant slumps and the Phoenician structures: Collapse  
881 features along the continental margin of the southeastern Mediterranean Sea, *Mar.*  
882 *Geophys. Res.*, 28, 297–307, <https://doi.org/10.1007/s11001-007-9032-7>, 2007.

883 Mart, Y., Eisin, B., and Folkman, Y.: The Palmahim structure - A model of  
884 continuous tectonic activity since the Upper Miocene in the Southeastern  
885 Mediterranean off Israel, *Earth Planet. Sci. Lett.*, 39, 328–334,  
886 [https://doi.org/10.1016/0012-821X\(78\)90018-3](https://doi.org/10.1016/0012-821X(78)90018-3), 1978.

887 Martinez, J. F., Cartwright, J., and Hall, B.: 3D seismic interpretation of slump  
888 complexes: Examples from the continental margin of Israel, *Basin Res.*, 17, 83–108,  
889 <https://doi.org/10.1111/j.1365-2117.2005.00255.x>, 2005.

890 Mascle, J., Zitter, T., Bellaiche, G., Droz, L., Gaullier, V., and Loncke, L.: The Nile  
891 deep sea fan: preliminary results from a swath bathymetry survey, *Mar. Pet. Geol.*, 18,  
892 471–477, [https://doi.org/10.1016/S0264-8172\(00\)00072-6](https://doi.org/10.1016/S0264-8172(00)00072-6), 2001.

893 Neev, D., Bakler, N., Moshkovitz, S., Kaufman, A., Magaritz, M., and Gofna, R.:  
894 Recent Faulting along the Mediterranean Coast of Israel, *Nature*, 245, 254–256,  
895 <https://doi.org/10.1038/245254a0>, 1973.

896 Neev, D.: Tectonic evolution of the Middle East and the Levantine basin (easternmost  
897 Mediterranean ), [https://doi.org/10.1130/00917613\(1975\)3<683:TEOTME>2.0.CO;2](https://doi.org/10.1130/00917613(1975)3<683:TEOTME>2.0.CO;2),  
898 1975.

899 Neev, D., Almagor, G., Arad, A., Ginzburg, A., and Hall, J. K.: The geology of the  
900 Southeastern Mediterranean Sea, GSI Report, 1–88 pp., 1976.

901 Netzeband, G. L., Hübscher, C. P., and Gajewski, D.: The structural evolution of the  
902 Messinian evaporites in the Levantine Basin, *Mar. Geol.*, 230, 249–273,  
903 <https://doi.org/10.1016/j.margeo.2006.05.004>, 2006.

904 On, G. N.: Guidance Notes on Subsea Pipeline Route Determination, 2016.

905 Perlin, A. and Kit, E.: Longshore Sediment Transport on Mediterranean Coast of  
906 Israel, *J. Waterw. Port, Coastal, Ocean Eng.*, 125, 80–87,  
907 [https://doi.org/10.1061/\(asce\)0733-950x\(1999\)125:2\(80\)](https://doi.org/10.1061/(asce)0733-950x(1999)125:2(80)), 1999.

908 Posamentier: Seismic stratigraphy into the next millen-  
909 data, 2000.

910 Prior, D. B. and Hooper, J. R.: Sea floor engineering geomorphology: Recent  
911 achievements and future directions, *Geomorphology*, 31, 411–439,  
912 [https://doi.org/10.1016/S0169-555X\(99\)00090-2](https://doi.org/10.1016/S0169-555X(99)00090-2), 1999.

913 Reches, Z. and Hoexter, D. F.: Holocene seismic and tectonic activity in the Dead Sea  
914 area, *Tectonophysics*, 80, 235–254, [https://doi.org/10.1016/0040-1951\(81\)90151-7](https://doi.org/10.1016/0040-1951(81)90151-7),  
915 1981.

916 Robertson, A. H. F.: Mesozoic-Tertiary tectonic evolution of the easternmost  
917 Mediterranean area: Integration of marine and land evidence, *Proceedings of the*  
918 *Ocean Drilling Program: Scientific Results*, 723–784 pp.,  
919 <https://doi.org/10.2973/odp.proc.sr.160.061.1998>, 1998.

920 Ryan, W. B. F. and Cita, M. B.: The nature and distribution of Messinian erosional  
921 surfaces - Indicators of a several-kilometer-deep Mediterranean in the Miocene, *Mar.*  
922 *Geol.*, 27, 193–230, [https://doi.org/10.1016/0025-3227\(78\)90032-4](https://doi.org/10.1016/0025-3227(78)90032-4), 1978.

923 Ryan, W. B. F. and Hsü, K. J.: Initial Report of the Deep-Sea Drilling Project, Leg  
924 XIII, US Gov. Print. Off. Washingt., 1973.

925 Sade, A. R., Hall, J. K., Amit, G., Golan, A., Gur-Arieh, L., and Tibor, G.: The Israel  
926 national bathymetric survey - A new look at the seafloor off Israel, *Isr. J. Earth Sci.*,  
927 55, 185–187, [https://doi.org/10.1560/IJES\\_55\\_3\\_185](https://doi.org/10.1560/IJES_55_3_185), 2006.

928 Sade, R., Hall, J. K., and Golan, A.: Multibeam bathymetry of the seafloor off  
929 Northern Israel, *Isr. Geol. Soc.*, 2007.

930 Safadi, M., Meilijson, A., and Makovsky, Y.: Internal deformation of the southeast  
931 Levant margin through continued activity of buried mass transport deposits,  
932 *Tectonics*, 36, 559–581, <https://doi.org/10.1002/2016TC004342>, 2017.

933 Sagy, Y., Gvirtzman, Z., and Reshef, M.: 80 m.y. of folding migration: New  
934 perspective on the Syrian arc from Levant Basin analysis, *Geology*, 46, 175–178,  
935 <https://doi.org/10.1130/G39654.1>, 2018.

936 Schattner, U. and Lazar, M.: Hierarchy of source-to-sink systems — Example from  
937 the Nile distribution across the eastern Mediterranean, *Sediment. Geol.*, 343, 119–  
938 131, <https://doi.org/10.1016/j.sedgeo.2016.08.006>, 2016.

939 Schattner, U., Ben-Avraham, Z., Lazar, M., and Hübscher, C.: Tectonic isolation of  
940 the Levant basin offshore Galilee-Lebanon - effects of the Dead Sea fault plate  
941 boundary on the Levant continental margin, eastern Mediterranean, *J. Struct. Geol.*,  
942 28, 2049–2066, <https://doi.org/10.1016/J.JSG.2006.06.003>, 2006.

943 Schattner, U., Gurevich, M., Kanari, M., and Lazar, M.: Levant jet system-effect of  
944 post LGM seafloor currents on Nile sediment transport in the eastern Mediterranean,  
945 *Sediment. Geol.*, 329, 28–39, <https://doi.org/10.1016/j.sedgeo.2015.09.007>, 2015.

946 Sharon, M., Sagy, A., Kurzon, I., Marco, S., and Rosensaft, M.: Assessment of  
947 seismic sources and capable faults through hierarchic tectonic criteria: Implications  
948 for seismic hazard in the Levant, *Nat. Hazards Earth Syst. Sci.*, 20, 125–148,  
949 <https://doi.org/10.5194/nhess-20-125-2020>, 2020.

950 Shmatkova, A. A., Shmatkov, A. A., Gainanov, V. G., and Buenz, S.: Identification of  
951 geohazards based on the data of marine high-resolution 3D seismic observations in  
952 the Norwegian Sea, *Moscow Univ. Geol. Bull.*, 70, 53–61,  
953 <https://doi.org/10.3103/S0145875215010068>, 2015.

954 Stanley, D. J.: Sediment transport on the coast and shelf between the Nile delta and

955 Israeli margin as determined by heavy minerals, *J. Coast. Res.*, 5, 813–828, 1989.

956 Steinberg, J., Gvirtzman, Z., Gvirtzman, H., and Ben-Gai, Y.: Late Tertiary faulting  
957 along the coastal plain of Israel, *Tectonics*, 27, n/a-n/a,  
958 <https://doi.org/10.1029/2007TC002151>, 2008.

959 Steinberg, J., Gvirtzman, Z., Folkman, Y., and Garfunkel, Z.: Origin and nature of the  
960 rapid late Tertiary filling of the Levant Basin, *Geology*, 39, 355–358,  
961 <https://doi.org/10.1130/G31615.1>, 2011.

962 Tibor, G., Ben-avraham, Z. V. I., Steckler, M., and Fligelman, H.: Subsidence History  
963 of the Southern Levant Margin , Eastern Mediterranean Sea , and Its Implications to  
964 the Understanding of the Messinian Event boundaries include the Dead Sea  
965 Transform to the east , the Cyprian arc to the northwest , mountains in the rel, 97,  
966 1992.

967 Tibor, G., Sade, R., and Hall, J. K.: Data collection and processing of multibeam data  
968 from the deep water offshore Israel, 2013.

969 Wells, D. L. and Coppersmith, K. J.: New Empirical Relationships among Magnitude,  
970 Rupture Length, Rupture Width, Rupture Area, and Surface Displacement, *Bulletin of*  
971 *the Seismological Society of America*, 974–1002 pp., 1994.

972 Wetzler, N. and Kurzon, I.: The Earthquake Activity of Israel: Revisiting 30 Years of  
973 Local and Regional Seismic Records along the Dead Sea Transform, *Seismol. Res.*  
974 *Lett.*, 87, 47–58, <https://doi.org/10.1785/0220150157>, 2016.

975 Wong, I.G. and Stepp, C.: Probabilistic seismic hazard analyses for fault displacement  
976 and vibratory ground motion at Yucca Mountain, Nevada. Milestone SP32IM3,  
977 September, 23, p.1998.

978 Youngs, R. R., Arabasz, W. J., Anderson, R. E., Ramelli, A. R., Ake, J. P., Slemmons,  
979 D. B., McCalpin, J. P., Doser, D. I., Fridrich, C. J., Swan, F. H., Rogers, A. M.,  
980 Yount, J. C., Anderson, L. W., Smith, K. D., Bruhn, R. L., Knuepfer, P. L. K., Smith,  
981 R. B., DePolo, C. M., O’Leary, D. W., Coppersmith, K. J., Pezzopane, S. K.,  
982 Schwartz, D. P., Whitney, J. W., Olig, S. S., and Toro, G. R.: A methodology for  
983 probabilistic fault displacement hazard analysis (PFDHA), *Earthq. Spectra*, 19, 191–  
984 219, <https://doi.org/10.1193/1.1542891>, 2003.

985 Zucker, E., Gvirtzman, Z., Granjeon, D., and Garcia-castellanos, D.: The accretion of  
986 the Levant continental shelf alongside the Nile Delta by immense margin-parallel  
987 sediment transport, *Mar. Pet. Geol.*, 126, 104876,  
988 <https://doi.org/10.1016/j.marpetgeo.2020.104876>, 2021.

989 Zviely, D., Sivan, D., Ecker, A., Bakler, N., Rohrlich, V., Galili, E., Boaretto, E.,  
990 Klein, M., and Kit, E.: Holocene evolution of the Haifa Bay area, Israel, and its  
991 influence on ancient tell settlements, *The Holocene*, 16, 849–861,  
992 <https://doi.org/10.1191/0959683606hol977rp>, 2006.

993 Zviely, D., Kit, E., and Klein, M.: Longshore sand transport estimates along the  
994 Mediterranean coast of Israel in the Holocene, *Mar. Geol.*, 238, 61–73,  
995 <https://doi.org/10.1016/j.margeo.2006.12.003>, 2007.

996

997